ASTRONOMY AND ASTROPHYSICS

Molecular envelopes around carbon stars

Interferometric observations and models of HCN and CN emission

M. Lindqvist[1,2], **F.L. Schöier**[3], **R. Lucas**[4], **and H. Olofsson**[3]

[1] Onsala Space Observatory, 439 92 Onsala, Sweden (michael@oso.chalmers.se)
[2] Sterrewacht Leiden, P.O. Box 9513, 2300 RA Leiden, The Netherlands
[3] Stockholm Observatory, 13336, Saltsjöbaden, Sweden (fredrik, hans@astro.su.se)
[4] IRAM, 300 rue de la Piscine, 38406 St Martin d'Heres Cedex, France (lucas@iram.fr)

Received 16 February 2000 / Accepted 8 August 2000

Abstract. We have observed four carbon stars (W Ori, RW LMi [CIT6], Y CVn, and LP And [IRC+40540]) in the HCN($J = 1 \rightarrow 0$) line and three of them (RW LMi, Y CVn, and LP And) also in the CN($N = 1 \rightarrow 0$) line using the IRAM interferometer on Plateau de Bure. The HCN brightness distributions are centred on the stellar positions suggesting a photospheric origin of this molecule. We see the expected structure of a hollow CN brightness distribution outside that of the HCN emitting region (in particular, for RW LMi and LP And).

We have used a non-LTE radiative transfer code, based on the Monte Carlo method, to model the circumstellar HCN and CN line emissions. We have, in addition to the interferometer data, used also multi-transition single dish data as constraints. The results are qualitatively, and in most cases also quantitatively, consistent with a simple photodissociation model, in which HCN is produced in the stellar atmosphere, while the observed CN is formed in the circumstellar envelope due to the photodissociation of HCN. The most notable discrepancy is the low CN/HCN peak abundance ratios, ≈0.16, obtained for those objects with the best observational constraints. These are lower by at least a factor of two compared to the results of also more elaborate chemical models. Some of our modelling discrepancies, e.g., the weakness of the model HCN($J = 1 \rightarrow 0$) intensities, are attributed to a too crude treatment of the radiative excitation in the inner region of a circumstellar envelope, and to a lack of knowledge of the density structure and kinematics in the same region. We find it particularly difficult to model the circumstellar line emissions towards RW LMi, and suspect that this is due to, e.g., a mass loss rate that has varied with time and/or a non-spherical envelope. The HCN and CN brightness maps suggest the latter.

Furthermore, we have obtained interferometric data towards RW LMi in also the HNC($J = 1 \rightarrow 0$), HC_3N($J = 10 \rightarrow 9$), HC_5N($J = 34 \rightarrow 33$) and SiS($J = 5 \rightarrow 4$) lines. The HNC, HC_3N, and HC_5N molecules appear to be distributed in a shell, while the SiS emission is clearly confined to regions close to the star. The HCN($J = 1 \rightarrow 0$), HNC($J = 1 \rightarrow 0$), and HC_3N($J = 10 \rightarrow 9$) lines show the effect that the peak brightness position varies systematically with the velocity. We attribute this to a large-scale asymmetry in the envelope. We also find that some of the spectra obtained towards the map centre are highly asymmetric, with the redshifted emission being significantly stronger than the blueshifted emission.

Key words: stars: circumstellar matter – stars: late-type – stars: AGB and post-AGB – stars: mass-loss – stars: carbon

Send offprint requests to: M. Lindqvist

1. Introduction

Asymptotic giant branch (AGB) stars often have massive circumstellar envelopes (CSEs) formed by intense mass loss during the very last phases of their evolution (Olofsson 1996). The CSEs consist of dust grains and gas, where the latter is mainly in molecular form as a consequence of chemical reactions in the stellar atmosphere as well as in the envelope itself. For various reasons, studies of circumstellar chemistry, while interesting in their own right, are moreover of great importance for understanding key processes of astrochemistry in general: the physical conditions span broad ranges in e.g. temperature and density, the geometry and kinematics are relatively well defined, the tenuous external parts of the CSEs favour a very active photochemistry, and the evolution of the central star leads to, sometimes drastic, changes in the physical conditions and hence the chemistry.

Circumstellar molecular line emission is an important tool for studying many aspects of the late stages of stellar evolution. Some of the molecular emissions are particularly suitable for estimating the mass loss properties of the stars, e.g., CO and OH, while other molecular abundances (including isotopic ratios) may be used to estimate elemental abundances, as well as other stellar properties. However, our knowledge of the small- and large-scale distribution of the molecules in CSEs (e.g., necessary for calculating reliable abundances) is rather limited, since only for a small sample of objects the emission regions of a few lines are resolved with single–dish observations. In principle, the only data with reasonable statistics and angular resolution are the interferometric CO (Neri et al. 1998) and SiO data (Lu-

Table 1. Source sample

Source	$\alpha(J2000.0)$	$\delta(J2000.0)$	Distance (pc)	Period (days)	L ($L_\odot$)	$\dot{M}$[4] ($M_\odot\,yr^{-1}$)	v_e[4] ($km\,s^{-1}$)	v_c[4] ($km\,s^{-1}$)	$^{12}CO/^{13}CO$[5]
W Ori	$05^h05^m23^s.72$	$01°10'39''.5$[1]	220	212	2600	7×10^{-8}	11.0	-1.0	–
CW Leo	09 47 57.33	13 16 43.4[2]	120	630	9600	1.5×10^{-5}	14.5	-26.5	50
RW LMi	10 16 02.35	30 34 19.0[3]	440	640	9700	6×10^{-6}	17.0	-1.0	35
Y CVn	12 45 07.83	45 26 24.9[1]	220	157	4400	1.5×10^{-7}	8.5	-22.5	2.5
LP And	23 34 27.71	43 33 02.2[2]	630	628	9400	1.5×10^{-5}	14.0	-16.0	55

[1] Hipparcos, [2] Becklin et al. (1969), [3] Claussen et al. (1987), [4] Schöier & Olofsson (2000b), [5] Schöier & Olofsson (2000a)

cas et al. 1992; Sahai & Bieging 1993), if we exclude data on OH and H_2O maser emission. For a number of species, e.g., CS, SiS, HNC, HC_3N, HC_5N, C_2H, C_3H, C_4H, C_3N, MgNC, and SiC_2, there exist high-quality interferometric maps, but only for one object, CW Leo [IRC+10216] (Bieging & Tafalla 1993; Dayal & Bieging 1993, 1995; Gensheimer et al. 1995; Guélin et al. 1993, 1997; Lucas et al. 1995; Lucas & Guélin 1999). Therefore, the size of the emitting region (i.e., the inner and outer radii of the emitting envelope), which is crucial in the calculation of the molecular abundance and which is often determined by the photodissociation of the molecules, has to be estimated using theoretical models (Olofsson et al. 1993b; Bujarrabal et al. 1994), and hence is very uncertain. Additionally, the size may depend on the particular transition in question, due to different excitation requirements (e.g., Bell 1993; Audinos et al. 1994; Wootten et al. 1994). The status of present day millimetre arrays makes it possible to determine not only the size of the emitting region in different molecular lines, but also the geometrical structure of the CSE, and hence the mass loss properties of the central star. Such observations may be used to compare with, and, hopefully, better constrain chemical models (e.g., Glassgold et al. 1986; Cherchneff et al. 1993; Cherchneff & Glassgold 1993; Millar & Herbst 1994; Willacy & Cherchneff 1998; Doty & Leung 1998; MacKay & Charnley 1999).

To improve upon this situation we present the results of interferometric measurements of HCN and CN line brightness distributions towards a sample of carbon stars, and in addition SiS, HNC, HC_3N and HC_5N line brightness distributions towards the high mass loss rate carbon star RW LMi. The chosen stars span quite a large range in mass loss rates, $10^{-7}-10^{-5}\ M_\odot\,yr^{-1}$. In order to make a quantitative analysis of the data we have used a non-LTE radiative transfer code, based on the Monte Carlo method, to model the circumstellar molecular line brightness distributions.

2. Observations and data reduction

In this section we present the sources, the observational equipment and procedure, and the data reduction. Some data on the sources are given in Table 1. The Hipparcos positions are given in the FK5 system (Equinox=$J2000.0$, Epoch=$J2000$) with proper motions taken into account as computed by VizieR (Ochsenbein 1997). If possible, we use Hipparcos distances. These tend to be smaller than the distances obtained by the method used by Olofsson et al. (1993a). We have also included the carbon star CW Leo in our sample for comparison. The HCN($J=1\rightarrow0$) and CN($N=1\rightarrow0$) data (Dayal & Bieging 1995) used for the modelling of CW Leo has been extracted from the Astronomy Digital Image Library[1]. The apparent bolometric fluxes used to estimate the luminosity of the stars have been obtained from Kerschbaum (private comm.); see Kerschbaum (1999) for a description of the method used.

2.1. Sources

2.1.1. W Orionis

W Ori (also known as IRC+00066, RAFGL 683, and IRAS 05028+0106) is a semiregular (SRb) carbon star with a period of 212 days. The Hipparcos distance is 220 pc. From the apparent bolometric flux we estimate that the luminosity is $2600\,L_\odot$. The spectral energy distribution (SED) can be modelled using a single blackbody of 2200 K, suggesting a low mass loss rate. The mass loss rate, $\dot{M}=7\times10^{-8}\ M_\odot\,yr^{-1}$, systemic velocity, $v_c=-1.0\,km\,s^{-1}$, and gas expansion velocity, $v_e=11.0\,km\,s^{-1}$, have been estimated from CO radio line data (Schöier & Olofsson 2000b; see also Sect. 4). W Ori was included in the molecular line survey of Olofsson et al. (1993a,b). It has a surprisingly strong HCN($J=1\rightarrow0$) line for its low mass loss rate. This is at least partly due to probable maser action in this line, as suggested by narrow features as well as time variability (Izumiura 1990; Olofsson et al. 1993b; Izumiura et al. 1995; Olofsson et al. 1998). In addition, the CN/HCN line intensity ratio is anomalously low (Bachiller et al. 1997). Thus, we have observed only the HCN($J=1\rightarrow0$) line towards this star.

2.1.2. CW Leonis

CW Leo (also know as IRC+10216, RAFGL 1381, and IRAS 09452+1330) is a wellknown Mira variable carbon star with a period of 630 days. In fact, it has by far most the well-studied AGB-CSE. Using the period-luminosity relation of Groenewegen et al. (1998) we estimate the luminosity to be $9600\,L_\odot$. The apparent bolometric magnitude gives a distance of 120 pc. The SED can be modelled using a single blackbody of 510 K. Using CO data Schöier & Olofsson (2000b)

[1] http://adil.ncsa.uiuc.edu

derived $\dot{M} = 1.5 \times 10^{-5}$ $\mathrm{M}_\odot\,\mathrm{yr}^{-1}$, $v_\mathrm{c} = -26.5\,\mathrm{km\,s}^{-1}$, and $v_\mathrm{e} = 14.5\,\mathrm{km\,s}^{-1}$ (see also Sect. 4). CW Leo was included in the survey of Olofsson et al. (1993a,b). We model here, for comparison, the interferometric HCN($1 \rightarrow 0$) and CN($N = 1 \rightarrow 0$) data obtained by Dayal & Bieging (1995).

2.1.3. RW Leonis Minoris

RW LMi (also known as IRC+30219, CIT6, RAFGL 1403, and IRAS 10131+3049) is a semiregular (SRa) carbon star with a period of 640 days. The period-luminosity relation for C-stars (Groenewegen & Whitelock 1996) gives a luminosity of $9700\,L_\odot$. Using this luminosity and the apparent bolometric flux we arrive at a distance of 440 pc. The SED can be modelled using two blackbodies with temperatures of 1000 K and 510 K, respectively. The ratio of the blackbody luminosities is 6.7, with the cooler one being the more luminous. Using CO data Schöier & Olofsson (2000b) derived $\dot{M} = 6 \times 10^{-6}$ $\mathrm{M}_\odot\,\mathrm{yr}^{-1}$, $v_\mathrm{c} = -1.0\,\mathrm{km\,s}^{-1}$, and $v_\mathrm{e} = 17.0\,\mathrm{km\,s}^{-1}$ (see also Sect. 4). This star appears very similar to CW Leo. It is relatively rich in detected circumstellar molecular species (e.g., CO, HCN, CN, HNC, $\mathrm{HC_3N}$, $\mathrm{HC_5N}$, $\mathrm{C_3N}$, and SiS; Jewell & Snyder 1982; Henkel et al. 1985; Sopka et al. 1989; Olofsson et al. 1993a,b; Fukasaku et al. 1994). Guilloteau et al. (1987) discovered a strong, vibrationally excited, masing HCN($J = 1 \rightarrow 0$) line. For this star we present HCN($J = 1 \rightarrow 0$), CN($N = 1 \rightarrow 0$), SiS($J = 5 \rightarrow 4$), HNC($J = 1 \rightarrow 0$), $\mathrm{HC_3N}$($J = 10 \rightarrow 9$), and $\mathrm{HC_5N}$($J = 34 \rightarrow 33$) brightness maps.

2.1.4. Y Canum Venaticorum

Y CVn (also known as IRC+50219, RAFGL 1576, and IRAS 12427+4542) is an SRb carbon star with a period of 157 days. It is the brightest (in the optical) known J-type carbon star [i.e., it is characterized by a low $^{12}\mathrm{C}/^{13}\mathrm{C}$-ratio in the stellar atmosphere, 3.5 (Lambert et al. 1986)]. The Hipparcos distance, 220 pc, is used in this paper. Using the apparent bolometric flux we arrive at a luminosity of $4400\,L_\odot$. The SED can be modelled using a single blackbody of 2200 K. Using CO data Schöier & Olofsson (2000b) derived $\dot{M} = 1.5 \times 10^{-7}$ $\mathrm{M}_\odot\,\mathrm{yr}^{-1}$, $v_\mathrm{c} = 22.5\,\mathrm{km\,s}^{-1}$, and $v_\mathrm{e} = 8.5\,\mathrm{km\,s}^{-1}$ (see also Sect. 4). Y CVn was included in the molecular line survey of Olofsson et al. (1993a,b). Izumiura et al. (1996) reported the presence of a large detached dust shell around this star. We present HCN($J = 1 \rightarrow 0$) and CN($N = 1 \rightarrow 0$) brightness maps.

2.1.5. LP Andromedae

LP And (also known as IRC+40540, RAFGL 3116, and IRAS 23320+4316) is an extremely reddened Mira variable carbon star with a period of 628 days (Cohen & Hitchon 1996). The period-luminosity relation for C-stars (Groenewegen & Whitelock 1996) gives a luminosity of $9400\,L_\odot$. Using this luminosity and the apparent bolometric flux we arrive at a distance of 630 pc. The SED can be modelled using two blackbodies with temperatures of 1100 K and 610 K, respectively. The ratio of the blackbody luminosities is 6.6, with the cooler one being the more luminous. Using CO data Schöier & Olofsson (2000b) derived $\dot{M} = 1.5 \times 10^{-5}$ $\mathrm{M}_\odot\,\mathrm{yr}^{-1}$, $v_\mathrm{c} = -16.0\,\mathrm{km\,s}^{-1}$, and $v_\mathrm{e} = 14.0\,\mathrm{km\,s}^{-1}$ (see also Sect. 4). Hence, in all respects it resembles RW LMi and CW Leo. It was not included in the molecular line survey of Olofsson et al. (1993a,b), but Sopka et al. (1989) have detected HCN and CN. We present HCN($J = 1 \rightarrow 0$) and CN($N = 1 \rightarrow 0$) brightness maps.

2.2. Observations

The observations were made using the IRAM interferometer (Guilloteau et al. 1992) on Plateau de Bure, France, between 1993 and 1995. During the time of our observations it changed from three to four 15 m diameter reflector antennae equipped with cooled SIS heterodyne receivers operating in the 3 mm window.

2.2.1. HCN

The HCN($J = 1 \rightarrow 0$) observations took place between February and July, 1993. We used the snap shot mode with the configurations C2, B2, and B3. This corresponds to baselines 24–300 m. We used about three observations (at different hour angles) per configuration, each one consisting of two integrating periods of 20 minutes, interspaced by four minute integrations on a phase calibrator. The bandwidth was 80 MHz, and the number of frequency points 128 (frequency separation 0.625 MHz) covering the HCN($J = 1 \rightarrow 0$) line at $\nu_0 = 88.632$ GHz.

2.2.2. CN

The CN($N = 1 \rightarrow 0$) observations at 113.3 GHz were also done in snap-shot mode, and they took place during 1993 and 1994. The bandwidth was 80 MHz, and the number of frequency points 128 (frequency separation 0.625 MHz). We covered all the hyperfine lines during the observations, but the analysis was done only for the lines not affected by blending in the low-frequency group.

2.2.3. SiS, HNC, $\mathrm{HC_3N}$ and $\mathrm{HC_5N}$

The observations of the SiS($J = 5 \rightarrow 4$; 90.772 GHz), HNC($J = 1 \rightarrow 0$; 90.662 GHz), $\mathrm{HC_3N}$($J = 10 \rightarrow 9$; 90.979 GHz) and $\mathrm{HC_5N}$($J = 34 \rightarrow 33$; 90.526 GHz) lines towards RW LMi were made during February and April, 1995. The configuration set was CD, which corresponds to a full synthesis. The bandwidth and frequency points were the same as for the HCN and CN observations.

2.3. Data reduction

The data were calibrated using the software package CLIC (Continuum and Line Interferometer Calibration), which is a dedicated package for calibration of Plateau de Bure interferometer data. For bandpass calibration we used either 3C345

or 3C273. In most cases we degraded the spectral resolution to $\approx 2.1\,\mathrm{km\,s^{-1}}$ prior to making maps. In the case of CN, we averaged, the 3 strongest hyperfine components not affected by blending, i.e., the $J = 1/2 \rightarrow 1/2$ group with relative weights 8, 8, and 10. We fitted models directly to the visibilities to obtain the best centre position prior to making maps. The results of this fitting process are the flux density and the position offsets in α and δ from the phase reference centre of the model source (normally a circular Gaussian). We then changed the phase tracking centre by applying an appropriate phase shift to the data. The errors obtained from the fit (see below) are the relative positional errors of the phase tracking centre of the array. The absolute positional rms are probably much larger. The position we obtained from the model is compared to the optical position (or other data) of the star, Table 1. The GILDAS (Grenoble Image and Line Data Analysis Software) package, the XS package (a spectral line reduction package developed by P. Bergman at Onsala Space Observatory), and the National Radio Astronomy Observatory AIPS (Astronomical Image Processing System) package, were used to produce maps and analyse the data. In most cases we used uniform weighting which gives higher resolution than natural weighting, but a lower S/N-ratio. The resulting resolution is ≈3–4″. The velocity scale is given with respect to the Local Standard of Rest (LSR). The typical rms in an emission free channel is about 10–$30\,\mathrm{mJy\,beam^{-1}}$, unless another value is given. The intensity scale, S, is given in $\mathrm{Jy\,beam^{-1}}$ which may be converted to brightness temperatures units, T_B, using

$$T_\mathrm{B} = \frac{S\lambda^2}{2k\Omega_B}, \tag{1}$$

where k is the Boltzmann constant, λ is the wavelength and Ω_B is the beam area given by,

$$\Omega_B = \frac{\pi\theta_\mathrm{major}\theta_\mathrm{minor}}{4\ln 2}, \tag{2}$$

where θ_major and θ_minor are the major and minor axis of the restoring beam.

3. Observational results on HCN and CN

In this section we present the observational results on HCN and CN. Each star is discussed in a separate sub-section. The size of the emitting region has been estimated by applying model fits to the data in the Fourier plane (Lucas et al. 1992), normally by assuming a circular Gaussian or a uniform disk brightness distribution. The fit is done independently for each channel. This may be a simplistic approach since some emissions show signs of asymmetry. Selected cleaned velocity-channel maps are presented in figures, as well as the synthesized CLEAN beam (shown at the half power contour) and the UV-plane coverage. Negative contours are dashed and zero is omitted for all contour plots in this Paper. We also present the velocity-integrated maps. Furthermore, for each map we present the spectrum at the map centre and the integrated spectrum (over the map). We have extracted radial brightness profiles by computing annular averages of the data close to the systemic velocity (typically around $v_\mathrm{c} \pm 2.1\,\mathrm{km\,s^{-1}}$). The width of each annulus is the pixel size in the map. This can be compared to the sizes obtained in the Fourier plane. For unresolved emissions the radial brightness profile only reflects the beam profile.

The integrated spectrum can be used to estimate the effect of missing flux by comparing with single–dish data. We have chosen to compare with Onsala 20 m telescope (OSO) data (see Tables 2 & 3). However, note that Table 3 gives the total integrated flux of the two hyperfine groups of the CN lines. To convert from T_A^* (K) to flux densities (Jy) we used conversion factors of 19.5 and 25.7 for HCN and CN, respectively. Note that the line intensities, integrated over velocity, in Tables 2 & 3 are given in the main beam brightness scale, i.e., the antenna temperature has been corrected for the atmospheric attenuation (using the chopper wheel method) and divided by the main beam efficiency. The latter is ≈ 0.6–0.5 (≈ 0.4–0.3 for data obtained before March 1993) in the frequency range 86–115 GHz for OSO data.

3.1. HCN towards W Ori

The HCN($J = 1 \rightarrow 0$) data obtained towards W Ori are presented in Fig. 1. The UV-coverage is rather poor with a baseline coverage of about 45–125 m, Fig. 1a. We have estimated the position of the HCN peak by fitting a circular Gaussian source model to the UV-data averaged over the velocity interval $-1.0 \pm 5.0\,\mathrm{km\,s^{-1}}$. The result is $\alpha(J2000) = 05^\mathrm{h}05^\mathrm{m}23\overset{\mathrm{s}}{.}70$ and $\delta(J2000) = 01°10'39\overset{''}{.}6$, which we adopt as the centre position. The error obtained from the model fit is about $0\overset{''}{.}1$ in α and δ, respectively. The position agrees, within the absolute positional uncertainty of $\leq 0\overset{''}{.}5$, with the Hipparcos position, $\alpha(J2000) = 05^\mathrm{h}05^\mathrm{m}23\overset{\mathrm{s}}{.}72$ and $\delta(J2000) = 01°10'39\overset{''}{.}5$. We have applied the same model to the high-resolution ($\Delta v \approx 0.5\,\mathrm{km\,s^{-1}}$) UV-data. There is no systematic variation of the position of the HCN peak across the line profile. The estimated half-power radius is $1\overset{''}{.}4 \pm 0\overset{''}{.}5$ at the systemic velocity ($-1.0 \pm 0.5\,\mathrm{km\,s^{-1}}$). We do not see the expected variation of the size of the envelope as a function of the line-of-sight velocity. Thus, our size estimate is most likely an upper limit due to the poor sampling. The cleaned velocity-channel maps show only unresolved emission. The rms in an emission free channel is about $60\,\mathrm{mJy\,beam^{-1}}$. We present only a velocity integrated map (from -14.2 to $+12.2\,\mathrm{km\,s^{-1}}$), Fig. 1b. The synthesized CLEAN beam, $4\overset{''}{.}4 \times 3\overset{''}{.}6$, is also shown. The position of the HCN peak in the image plane is consistent with the result obtained with the method described above. Both the line profile at the centre pixel and the integrated line profile (over the map) show narrow features (very likely of maser origin) at the blue- and red-shifted edges of the emission, Figs 1c and d. We have used the integrated line profile, Fig. 1d, for a comparison with single–dish data. The flux density (from -14.2 to $+12.2\,\mathrm{km\,s^{-1}}$) is $\approx 56\,\mathrm{Jy\,km\,s^{-1}}$. We estimate that the single–dish flux is $\approx 53\,\mathrm{Jy\,km\,s^{-1}}$ (based on OSO observations, Table 2). Thus, we may conclude that the map contains all of the HCN emission (even with a limited set of observations).

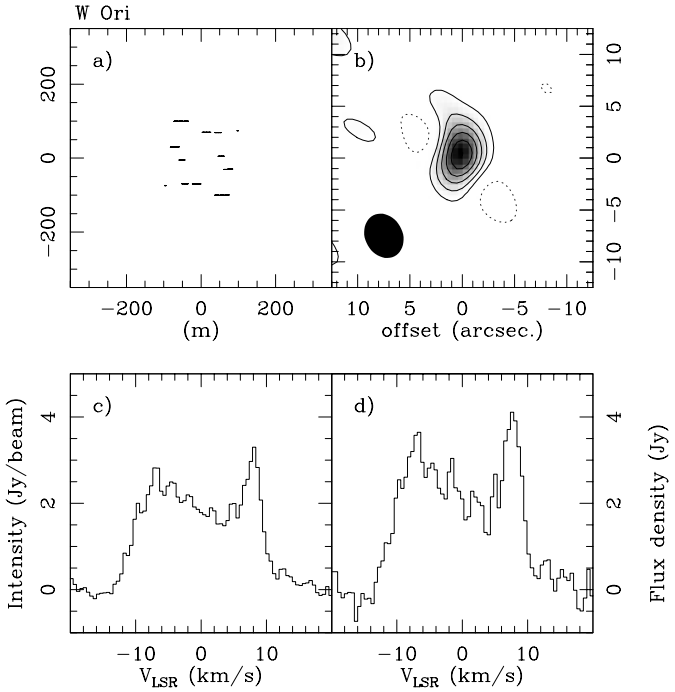

Fig. 1a–d. Results for W Ori. **a** The UV-plane coverage for the $\mathrm{HCN}(J=1\rightarrow0)$ observations. **b** Velocity integrated map (from -14.2 to $+12.2\,\mathrm{km\,s^{-1}}$) of the $\mathrm{HCN}(J=1\rightarrow0)$ line emission using natural weighting. The pixel size is $0\farcs5\times0\farcs5$. The coordinates are relative to $\alpha(J2000)=05^{\mathrm{h}}05^{\mathrm{m}}23\fs70$ and $\delta(J2000)=01^{\circ}10'39\farcs6$. The contours range from -15 to 90 by $15\,\mathrm{Jy\,beam^{-1}km\,s^{-1}}$; the peak value is $90.5\,\mathrm{Jy\,beam^{-1}km\,s^{-1}}$ (zero is omitted, and dashed contours are negative in all contour plots in this Paper). The synthesized CLEAN beam [shown at the half power contour (filled) in the lower left corner] is $4\farcs4\times3\farcs6$ with a position angle of 27°. **c** Interferometer $\mathrm{HCN}(J=1\rightarrow0)$ spectrum at the map centre ($\Delta v\approx0.5\,\mathrm{km\,s^{-1}}$); $1.0\,\mathrm{Jy\,beam^{-1}}$ corresponds to a brightness temperature of 9.8 K. **d** Integrated (over the maps) interferometer $\mathrm{HCN}(J=1\rightarrow0)$ spectrum ($\Delta v\approx0.5\,\mathrm{km\,s^{-1}}$).

3.2. HCN and CN towards RW LMi

The $\mathrm{HCN}(J=1\rightarrow0)$ and $\mathrm{CN}(N=1\rightarrow0)$ data towards RW LMi are presented in Fig. 2. The resulting UV-coverages for the HCN and CN observations are shown in Figs 2a and 2c, respectively. Using a circular Gaussian model to fit the data in the Fourier plane we find evidence for a systematic variation of the position of the HCN peak across the line profile, both in α and δ. Similar results have been obtained for some of the other emissions and the reason for this is discussed below (see Sect. 6.6). As a consequence, we have chosen the position of the continuum emission as the reference position for the HCN channel maps as well as for the maps of the other emissions (see Sect. 6.1). The adopted centre position is $\alpha(J2000)=10^{\mathrm{h}}16^{\mathrm{m}}02\fs28\,\delta(J2000)=30^{\circ}34'18\farcs9$, while the position of the HCN peak position at the systemic velocity is $\alpha(J2000)=10^{\mathrm{h}}16^{\mathrm{m}}02\fs38$ and $\delta(J2000)=30^{\circ}34'17\farcs4$. Nevertheless, the estimated size does vary with line-of-sight velocity as expected (within the errors), i.e., it is largest at the systemic velocity where we find a half power radius of $4\farcs6\pm0\farcs1$ (in the velocity interval $-1.0\pm2.1\,\mathrm{km\,s^{-1}}$). The HCN emission in the velocity-channel maps, where the synthesized CLEAN beam is $3\farcs1\times1\farcs9$, is resolved, Fig. 2b. Even though the images show the expected structure, a closer look at the HCN brightness distributions suggest some departures from spherical symmetry; the emission appears to be elongated with a position angle, PA, of about -25° (PA is counted from north to east). The line profile at the centre pixel and the integrated line profile (over the map), Figs 2g and i, have similar rounded shapes suggesting optically thick emission. The asymmetry of the line profiles can be explained by the three hyperfine components of the $J=1\rightarrow0$ transition. The radial brightness profile (around the systemic velocity, $-1.0\pm2.1\,\mathrm{km\,s^{-1}}$), Fig. 2k (solid line), cannot be fitted with a simple Gaussian. It shows extended emission at about $4''$ from the adopted centre position (a similar result has been obtained towards CW Leo; Dayal & Bieging 1995). The result of the model fit in the Fourier plane is probably an overestimate compared to the radial brightness distribution. The flux density in the integrated (from -24.1 to $+22.2\,\mathrm{km\,s^{-1}}$) line profile (over the map), Fig. 2i, is about $393\,\mathrm{Jy\,km\,s^{-1}}$. We estimate that the single–dish flux is $\approx342\,\mathrm{Jy\,km\,s^{-1}}$ (based on OSO observations, Table 2), which is within the calibration uncertainty of the single–dish/interferometer observations (about 20% each). Thus, we may conclude that the map contains all of the $\mathrm{HCN}(J=1\rightarrow0)$ emission.

We have not obtained a reliable estimate of the size in the Fourier plane of the CN brightness distribution at the the systemic velocity. The reason is the rather complicated structure of the emission seen in the images. The CN emission in the velocity-channel maps, where the synthesized CLEAN beam is $3\farcs7\times2\farcs8$, is clearly resolved, Fig. 2d. It outlines, as expected, a hollow shell. This is also clearly seen in the radial brightness distribution, and it is indicated by the highly double-peaked spectrum obtained towards the centre pixel. The size varies as a function of the line-of-sight velocity, i.e., it is largest at the systemic velocity. There is a clear elongation at PA $\approx-25^{\circ}$, i.e., in the same direction as the HCN emission. The brightness distribution is strongest in the NE and open towards the W. The radial brightness profile (derived around the systemic velocity, $-1.0\pm2.1\,\mathrm{km\,s^{-1}}$), Fig. 2k (dotted line), indicates that the peak emission occurs at about $5\farcs4$ from the adopted centre position. The spectrum at the map centre is asymmetric with the red-shifted emission stronger than the blue-shifted one, Fig. 2h. The flux density in the integrated (from -24.1 to $+22.2\,\mathrm{km\,s^{-1}}$) line profile, Fig. 2j, is about $45\,\mathrm{Jy\,km\,s^{-1}}$. We estimate that the single–dish flux is $\approx94\,\mathrm{Jy\,km\,s^{-1}}$ [based on OSO observations; note that the interferometer fluxes for CN in this paper is an average of the three strongest hyperfine lines in the low frequency hyperfine group of the $\mathrm{CN}(N=1\rightarrow0)$ transition; see above]. This discrepancy is larger than the calibration uncertainty in the single dish/interferometer data, and we conclude that some of the $\mathrm{CN}(N=1\rightarrow0)$ emission is missed by the interferometer.

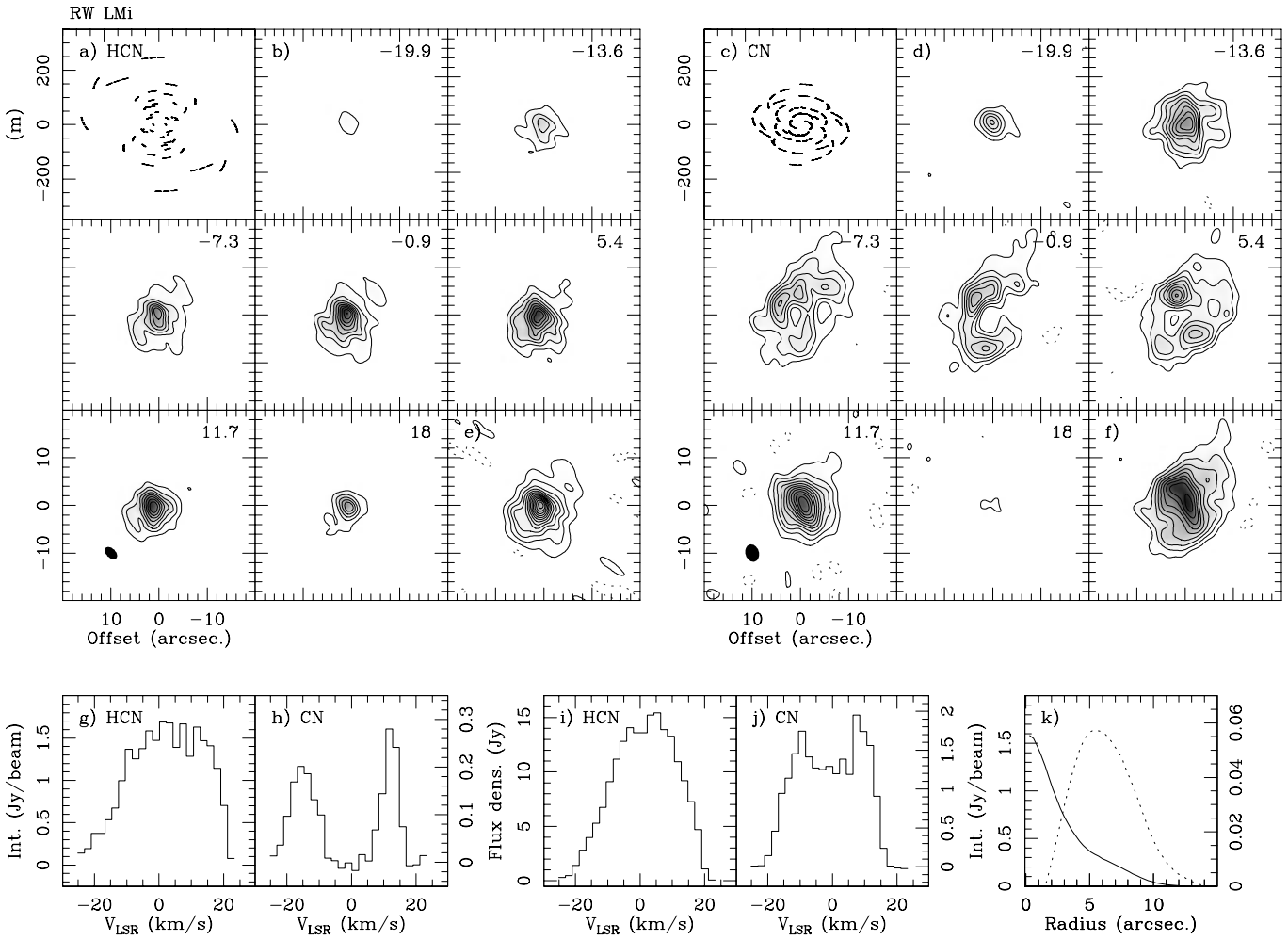

Fig. 2a–k. Results for RW LMi. **a** The UV-plane coverage for the HCN($J = 1 \rightarrow 0$) observations. **b** Velocity-channel maps ($\Delta v \approx 6.3\,\mathrm{km\,s^{-1}}$) of the HCN($J = 1 \rightarrow 0$) line emission using uniform weighting. The pixel size is $0\farcs3 \times 0\farcs3$. The coordinates are relative to $\alpha(J2000) = 10^{\mathrm{h}}16^{\mathrm{m}}02\fs28$ and $\delta(J2000) = 30^\circ34'18\farcs9$. The central LSR velocity of each channel is given in the upper right corner. The contours range from -0.4 to 2.0 by $0.2\,\mathrm{Jy\,beam^{-1}}$. The peak value is $2.1\,\mathrm{Jy\,beam^{-1}}$, and $1.0\,\mathrm{Jy\,beam^{-1}}$ corresponds to a brightness temperature of 26.4 K. The synthesized CLEAN beam is $3\farcs1 \times 1\farcs9$ with a position angle of 45°. **c** The UV-plane coverage for the CN($N = 1 \rightarrow 0$) observations. **d** Velocity-channel maps of the CN($N = 1 \rightarrow 0$) line emission. The contours range from -0.06 to 0.30 by $0.02\,\mathrm{Jy\,beam^{-1}}$. The peak value is $0.3\,\mathrm{Jy\,beam^{-1}}$, and $1.0\,\mathrm{Jy\,beam^{-1}}$ corresponds to a brightness temperature of 9.1 K. The synthesized CLEAN beam is $3\farcs7 \times 2\farcs8$ with a position angle of -163°. The rest as in Fig. 2b. **e** Velocity integrated map (from -24.1 to $22.2\,\mathrm{km\,s^{-1}}$) of the HCN($J = 1 \rightarrow 0$) line emission. The contours range from -3 to 27 by $2\,\mathrm{Jy\,beam^{-1}km\,s^{-1}}$; the peak value is $26.2\,\mathrm{Jy\,beam^{-1}km\,s^{-1}}$. **f** Velocity integrated map (from -24.1 to $22.2\,\mathrm{km\,s^{-1}}$) of the CN($N = 1 \rightarrow 0$) line emission. The contours range from -0.4 to 2.0 by $0.2\,\mathrm{Jy\,beam^{-1}km\,s^{-1}}$; the peak value is $1.9\,\mathrm{Jy\,beam^{-1}km\,s^{-1}}$. **g-h** Interferometer HCN($J = 1 \rightarrow 0$) and CN($N = 1 \rightarrow 0$) spectra at the map centre ($\Delta v \approx 2.1\,\mathrm{km\,s^{-1}}$). **i-j** Integrated (over the maps) interferometer HCN($J = 1 \rightarrow 0$) and CN($N = 1 \rightarrow 0$) spectra ($\Delta v \approx 2.1\,\mathrm{km\,s^{-1}}$). **k** The radial brightness profiles of the HCN($1 \rightarrow 0$) (solid line) and CN($N = 1 \rightarrow 0$) (dashed line) emission close to the systemic velocity ($-1.0 \pm 2.1\,\mathrm{km\,s^{-1}}$).

3.3. HCN and CN towards Y CVn

The HCN($J = 1 \rightarrow 0$) and CN($N = 1 \rightarrow 0$) data towards Y CVn are presented in Fig. 3. The resulting UV-coverages are shown in Figs 3a and 3d, respectively. We have estimated the position of the HCN peak by averaging the UV-data in the velocity interval $+22.0 \pm 2.1\,\mathrm{km\,s^{-1}}$. The result, using a circular Gaussian brightness distribution to fit the data, is $\alpha(J2000) = 12^{\mathrm{h}}45^{\mathrm{m}}07\fs84$ and $\delta(J2000) = 45^\circ26'24\farcs8$, which we adopt as the centre position. The error obtained from the model fit is $0\farcs02$ in both α and δ. The position agrees, within the absolute positional uncertainty of $\leq 0\farcs5$, with the Hipparcos position, $\alpha(J2000) = 12^{\mathrm{h}}45^{\mathrm{m}}07\fs83$ and $\delta(J2000) = 45^\circ26'24\farcs9$. By applying the same model to individual channels ($\Delta v \approx 2.1\,\mathrm{km\,s^{-1}}$), we find no systematic variation of the position of the HCN peak across the line profile. The estimated half-power radius is $0\farcs5 \pm 0\farcs05$ (in the velocity interval $+22.0 \pm 2.1\,\mathrm{km\,s^{-1}}$). The estimated size varies as a function of the line-of-sight velocity in the expected manner (within the considerable uncertainties). As in the case of W Ori the HCN emission in the velocity channel maps is unresolved. In this case we present a

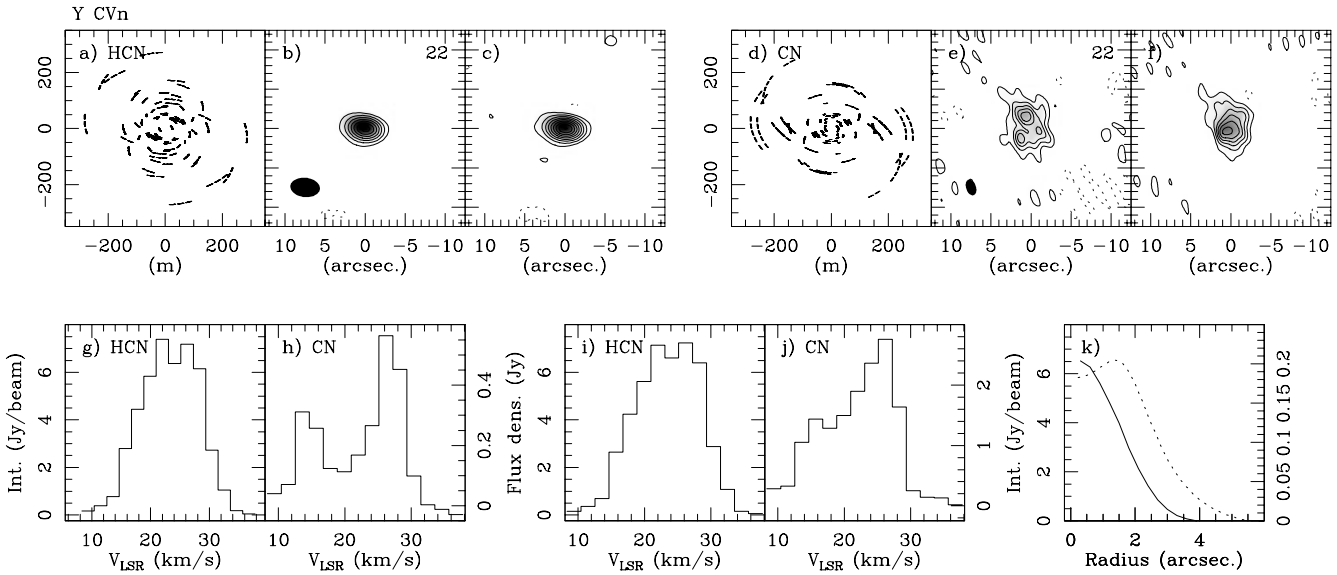

Fig. 3a–k. Results for Y CVn. **a** The UV-plane coverage for the $\mathrm{HCN}(J=1\rightarrow0)$ observations. **b** Velocity-channel map ($\Delta v\approx2.1\,\mathrm{km\,s^{-1}}$) at the systemic velocity ($22.0\,\mathrm{km\,s^{-1}}$) of the $\mathrm{HCN}(J=1\rightarrow0)$ line emission using uniform weighting. The pixel size is $0\farcs3\times0\farcs3$. The coordinates are relative to $\alpha(J2000)=12^{\mathrm{h}}45^{\mathrm{m}}07\fs84$ and $\delta(J2000)=45^{\circ}26'24\farcs8$. Contours range from -1.0 to 7.0 by $1.0\,\mathrm{Jy\,beam^{-1}}$. The peak value is $7.4\,\mathrm{Jy\,beam^{-1}}$, and $1.0\,\mathrm{Jy\,beam^{-1}}$ corresponds to a brightness temperature of 16.9 K. The synthesized CLEAN beam is $3\farcs7\times2\farcs5$ with a position angle of 83°. **c** Velocity integrated map (from 9.4 to $36.7\,\mathrm{km\,s^{-1}}$) of the $\mathrm{HCN}(J=1\rightarrow0)$ line emission. The contours range from -5 to 45 by $5\,\mathrm{Jy\,beam^{-1}km\,s^{-1}}$, and the peak value is $45.5\,\mathrm{Jy\,beam^{-1}km\,s^{-1}}$. **d** The UV-plane coverage for the $\mathrm{CN}(N=1\rightarrow0)$ observations. **e** Velocity-channel map at the systemic velocity of the $\mathrm{CN}(N=1\rightarrow0)$ line emission using uniform weighting. The pixel size is $0\farcs2\times0\farcs2$. Contours range from -0.15 to 0.55 by $0.05\,\mathrm{Jy\,beam^{-1}}$. The peak value is $0.6\,\mathrm{Jy\,beam^{-1}}$, and $1.0\,\mathrm{Jy\,beam^{-1}}$ corresponds to a brightness temperature of 36.9 K. The synthesized CLEAN beam is $2\farcs1\times1\farcs3$ with a position angle of -163°. The rest as in Fig. 3b. **f** Velocity integrated map (from 9.4 to $36.7\,\mathrm{km\,s^{-1}}$) of the $\mathrm{CN}(N=1\rightarrow0)$ line emission. The contours range from -0.4 to 2.4 by $0.4\,\mathrm{Jy\,beam^{-1}km\,s^{-1}}$, and the peak value is $2.6\,\mathrm{Jy\,beam^{-1}km\,s^{-1}}$. **g-h** Interferometer $\mathrm{HCN}(J=1\rightarrow0)$ and $\mathrm{CN}(N=1\rightarrow0)$ spectra at the map centre ($\Delta v\approx2.1\,\mathrm{km\,s^{-1}}$). **i-j** Integrated (over the maps) interferometer $\mathrm{HCN}(J=1\rightarrow0)$ and $\mathrm{CN}(N=1\rightarrow0)$ spectra ($\Delta v\approx2.1\,\mathrm{km\,s^{-1}}$). **k** The radial brightness profiles of the $\mathrm{HCN}(J=1\rightarrow0)$ (solid line) and $\mathrm{CN}(N=1\rightarrow0)$ (dashed line) emission close to the systemic velocity ($22.0\pm2.1\,\mathrm{km\,s^{-1}}$).

velocity integrated map (from $+9.4$ to $+36.7\,\mathrm{km\,s^{-1}}$) and a velocity channel map at the systemic velocity ($\Delta v\approx2.1\,\mathrm{km\,s^{-1}}$), Fig. 3b and c. The synthesized CLEAN beam, $3\farcs7\times2\farcs5$, is also shown. The position of the HCN peak, in the image plane, is consistent with the result obtained above. The line profile at the centre pixel, Fig. 3g, and the integrated line profile (over the map), Fig. 3i, have similar rounded shapes suggesting optically thick emission, but the hyperfine structure affects the shape. Since we are not resolving the emission, the radial brightness profile presented in Fig. 3k (solid line), integrated over the velocity interval $+22.0\pm2.1\,\mathrm{km\,s^{-1}}$, merely reflects the beam profile. Hence, we cannot compare with the size estimate obtained from the model fit in the Fourier plane. The flux density in the integrated line profile, Fig. 3i, (from 9.4 to $36.7\,\mathrm{km\,s^{-1}}$) is $\approx95\,\mathrm{Jy\,km\,s^{-1}}$. We estimate that the single–dish flux is $\approx108\,\mathrm{Jy\,km\,s^{-1}}$ (Table 2). Thus, we may conclude that within the measurement errors the map contains most of the HCN emission.

A crude estimate of the size of the CN brightness distribution has been obtained by applying a uniform disk brightness distribution model to the data in the Fourier plane. The size varies as a function of the line-of-sight velocity as expected, i.e., it is largest at the systemic velocity. The estimated diameter is $5\farcs9\pm0\farcs1$ close to the systemic velocity ($22.0\pm2.1\,\mathrm{km\,s^{-1}}$). The CN emission at the systemic velocity is at least partly resolved and we marginally detect a hollow shell distribution (assuming the same centre position as for HCN), Fig. 3e. The width of the shell is not resolved (the beam is $3\farcs7\times2\farcs5$). This is also shown in the radial brightness profile (around the systemic velocity, $22.0\pm2.1\,\mathrm{km\,s^{-1}}$), Fig. 3k. The peak occurs at about $1\farcs4$ from the adopted centre position. The CN brightness distribution in the maps is inconsistent with the model applied in the Fourier plane. Compared to the radial brightness profile, the size obtained from the model is probably a slight overestimate of the true distribution. The integrated line profile is asymmetric with the red-shifted emission stronger than the blue-shifted one, Fig. 3j. The spectrum at the map centre has a similar asymmetry and the horns at the extreme velocities show the characteristic of emission from an (at least partly) resolved shell, Fig. 3h. The flux density in the integrated (from 9.4 to $36.7\,\mathrm{km\,s^{-1}}$) line profile is about $32\,\mathrm{Jy\,km\,s^{-1}}$. We estimate that the single–dish flux is $\approx29\,\mathrm{Jy\,km\,s^{-1}}$ (based on OSO data). Thus, we may conclude that within the measurement errors the map contains all of the CN emission.

3.4. HCN and CN towards LP And

The $\mathrm{HCN}(J=1\rightarrow0)$ and $\mathrm{CN}(N=1\rightarrow0)$ data towards LP And are shown in Fig. 4. The resulting UV-coverages are shown

in Figs 4a and 4c, respectively. We have estimated the position of the HCN peak by averaging UV-data in the velocity interval $-16.0 \pm 2.1\,\mathrm{km\,s^{-1}}$. The result, using a Gaussian model to fit the data, is $\alpha(J2000) = 23^{\mathrm{h}}34^{\mathrm{m}}27\overset{\mathrm{s}}{.}51$ and $\delta(J2000) = 43^{\circ}33'01\overset{''}{.}6$, which we adopt as the centre position. The error obtained from the Gaussian model fit is $\approx 0\overset{''}{.}03$ both in α and δ. It is close to (within the absolute positional uncertainty of $\leq 0\overset{''}{.}5$) the best published IR position (with an uncertainty of $3''$), $\alpha(J2000) = 23^{\mathrm{h}}34^{\mathrm{m}}27\overset{\mathrm{s}}{.}71$ and $\delta(J2000) = 43^{\circ}33'02\overset{''}{.}2$ (Claussen et al. 1987), as well as with the CO($J = 1 \rightarrow 0$) peak position found by Neri et al. (1998), $\alpha(J2000) = 23^{\mathrm{h}}34^{\mathrm{m}}27\overset{\mathrm{s}}{.}43$ and $\delta(J2000) = 43^{\circ}33'01\overset{''}{.}9$. The model fitting suggests no systematic variation of the position of the HCN peak as a function of the velocity. The estimated size varies with line-of-sight velocity as expected (within the errors), i.e., it is largest at the systemic velocity where we find a half power radius of $2\overset{''}{.}5 \pm 0\overset{''}{.}1$. The HCN emission in the velocity-channel maps, where the synthesized CLEAN beam is $3\overset{''}{.}3 \times 1\overset{''}{.}9$, is resolved and appears to be spherically symmetric, Fig. 4b. The position of the HCN peak, in the image plane, is consistent with the results obtained above. The radial brightness profile (around the systemic velocity, $-16.0 \pm 2.1\,\mathrm{km\,s^{-1}}$) presented in Fig. 4k (solid line) can be fitted with a Gaussian with a radius of $2\overset{''}{.}6 \pm 0\overset{''}{.}2$, i.e., consistent with the result of the model fit in the Fourier plane. The centre pixel and integrated spectra, Figs 4g and i, suggest optically thick emission. We have used the integrated line profile, Fig. 4i, for a comparison with single–dish data. The flux density (from -32.9 to $+7.1\,\mathrm{km\,s^{-1}}$) is about $123\,\mathrm{Jy\,km\,s^{-1}}$. We estimate that the single–dish flux is $\approx$101 $\mathrm{Jy\,km\,s^{-1}}$ (based on OSO data, Table 2). The discrepancy is within the calibration uncertainty of the single–dish/interferometer observations. Thus, we may conclude that the map contains most of the HCN emission.

We have fitted a disk brightness distribution model to the CN UV-data. The size varies as a function of the line-of-sight velocity in the expected manner, i.e., it is largest at the systemic velocity ($-16.1 \pm 2.1\,\mathrm{km\,s^{-1}}$), where the estimated diameter is $12\overset{''}{.}1 \pm 0\overset{''}{.}3$. The CN emission in the velocity-channel maps presented in Fig. 4d is resolved and appears to be spherically symmetric, but the brightness distribution is rather patchy, suggesting some degree of clumpiness of the medium (the synthesized CLEAN beam is $4\overset{''}{.}0 \times 2\overset{''}{.}3$). Furthermore, there is evidence of the expected hollow shell distribution (assuming the same centre position as for HCN). The width of the shell is unresolved. The radial brightness profile suggests that the peak emission occurs at about $3\overset{''}{.}3$ from the adopted centre position. The spectrum at the map centre shows horns at the extreme velocities, which is characteristic of emission from an (at least partly) resolved shell, Fig. 4h. The integrated line profile has a rounded shape, though asymmetric, suggesting optically thick emission, Fig. 4j. We have used the integrated line profile for a comparison with single–dish data. The integrated flux density (from -32.9 to $-1.3\,\mathrm{km\,s^{-1}}$) is about $37\,\mathrm{Jy\,km\,s^{-1}}$. We estimate that the single–dish flux is $\approx$27 $\mathrm{Jy\,km\,s^{-1}}$ (based on OSO data). The discrepancy is about 30%, which is within the calibration uncertainty of the single–dish/interferometer observations. Thus, we may conclude that the map contains most of the CN emission.

4. Circumstellar model and radiative transfer

We have developed a non-LTE radiative transfer code, based on the Monte Carlo method, to derive some basic physical properties of the CSEs under study, and to model the observations presented in this paper. Assuming a spherically symmetric, expanding envelope the code calculates the molecular excitation, i.e., the level populations, needed to solve the radiative transfer equation exactly. The kinetic gas temperature is calculated by solving the energy balance equation, considering the most important heating and cooling mechanisms, including heating by dust-gas collisions and cooling by CO using the derived level populations [see Schöier (2000) for details].

The modelling of the CO emission observed towards these sources, as presented in Schöier & Olofsson (2000b), results in estimates of some of the basic parameters of the CSEs, such as the mass loss rate, the expansion velocity, and the radial kinetic temperature distribution of the gas. The three (in some cases four) lowest rotational transitions of CO were used in the analysis. The data were collected using the Onsala 20 m telescope (OSO), the Swedish-ESO submillimetre telescope (SEST), the IRAM 30 m telescope, the NRAO 12 m telescope, and the JCMT. The derived model CO intensities are generally consistent with the observations, and we believe that the derived mass loss rates are accurate to within a factor of two (neglecting the errors introduced in the adopted distances). However, we note that the CO envelope around RW LMi may have properties that differ from those of our simple circumstellar model, e.g., the mass loss rate may have been varying in time and there may be substantial deviations from sphericity. The estimated mass loss rates and expansion velocities of our sample stars are presented in Table 1, and these are the values, together with the derived kinetic temperature distributions (shown in Fig. 7 for the radial range relevant to the HCN and CN emission discussed here), which are used in the analysis of the HCN and CN emissions.

We define the fractional abundance, f_{X}, of a molecular species, X, as $f_{\mathrm{X}}(r) = n(\mathrm{X})/n(\mathrm{H_2})$, i.e., its number density relative to that of molecular hydrogen. We will here assume that the radial abundance distributions of HCN and CN can be represented by Gaussian functions. This will give slightly different distributions than those derived from the photodissociation model below, but due to the limitations of our observations, we find it reasonable to use this somewhat simpler description. For HCN we use

$$f_{\mathrm{HCN}}(r) = f_0\, e^{-(r/r_{\mathrm{e}})^2}, \tag{3}$$

where f_0 is the initial (photospheric) abundance of HCN and r_{e} is the e-folding distance, i.e., the radius where the abundance of HCN is f_0/e. For CN we use

$$f_{\mathrm{CN}}(r) = f_{\mathrm{p}}\, e^{-4[(r-r_{\mathrm{p}})/\Delta r]^2}, \tag{4}$$

where f_{p} is the peak CN abundance, r_{p} the radius of the peak abundance, and Δr is the full width of the shell at the e-folding

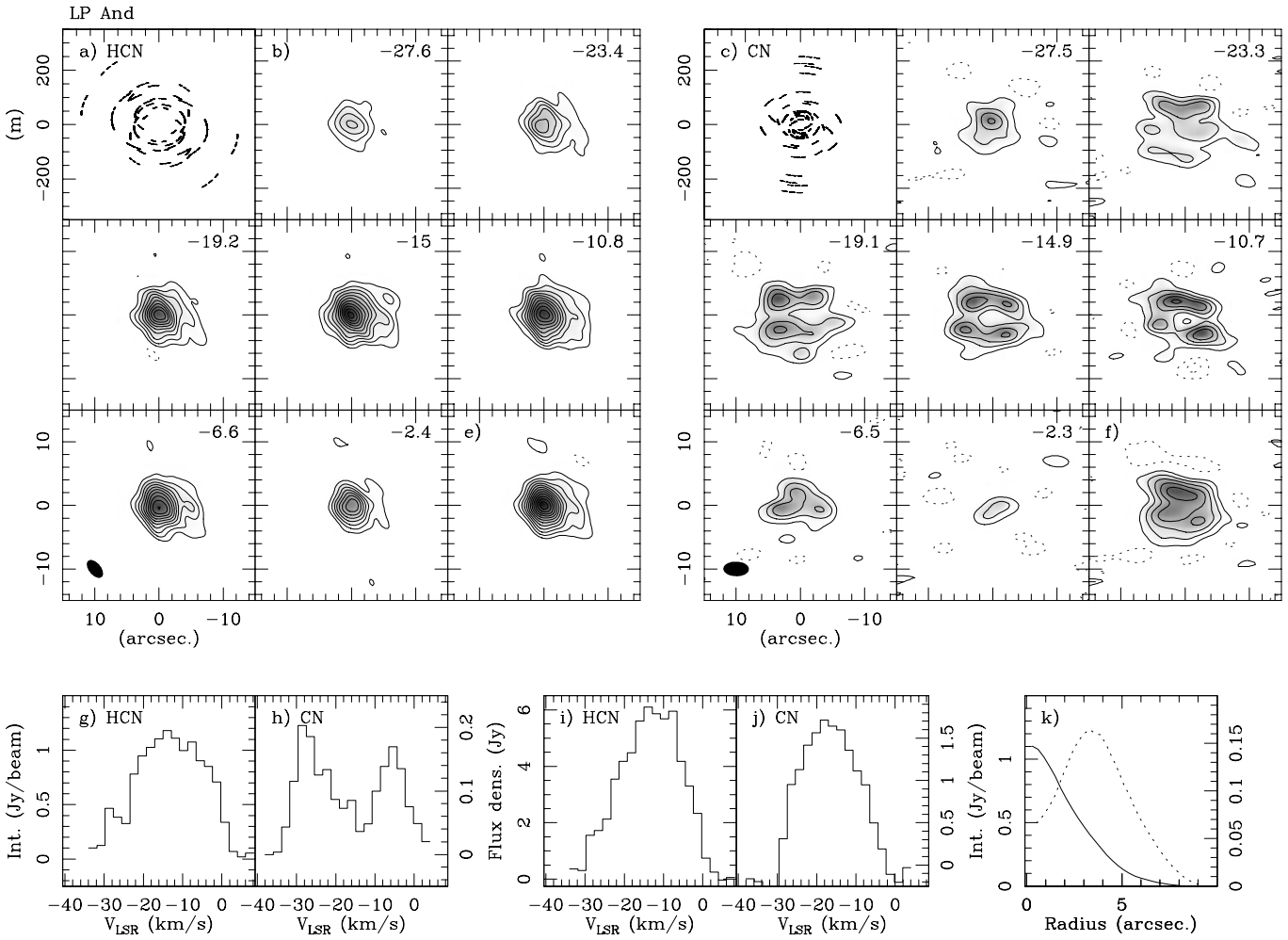

Fig. 4a–k. Results for LP And. **a** The UV-plane coverage for the HCN($J = 1 \rightarrow 0$) observations. **b** Velocity-channel maps ($\Delta v \approx 4.2\,\mathrm{km\,s^{-1}}$) of the HCN($J = 1 \rightarrow 0$) line emission using uniform weighting. The pixel size is $0\farcs3 \times 0\farcs3$. The coordinates are relative to $\alpha(J2000) = 23^{\mathrm{h}}34^{\mathrm{m}}27\fs51$ and $\delta(J2000) = 43^{\circ}33'01\farcs6$. Contours range from -0.3 to 1.2 by $0.10\,\mathrm{Jy\,beam^{-1}}$. The peak value is $1.2\,\mathrm{Jy\,beam^{-1}}$, and $1.0\,\mathrm{Jy\,beam^{-1}}$ corresponds to a brightness temperature of 25.5 K. The synthesized CLEAN beam is $3\farcs3 \times 1\farcs9$ with a position angle of 39°. **c** The UV-plane coverage for the CN($N = 1 \rightarrow 0$) observations. **d** Velocity-channel maps of the CN($N = 1 \rightarrow 0$) line emission. Contours range from -0.15 to 0.3 by $0.05\,\mathrm{Jy\,beam^{-1}}$. The peak value is $0.3\,\mathrm{Jy\,beam^{-1}}$, and $1.0\,\mathrm{Jy\,beam^{-1}}$ corresponds to a brightness temperature of 10.4 K. The synthesized CLEAN beam is $4\farcs0 \times 2\farcs3$ with a position angle of 89°. The rest as in Fig. 4b. **e** Velocity integrated map (from 9.4 to $36.7\,\mathrm{km\,s^{-1}}$) of the HCN($J = 1 \rightarrow 0$) line emission. The contours range from -2 to 13 by $1\,\mathrm{Jy\,beam^{-1}km\,s^{-1}}$, and the peak value is $12.6\,\mathrm{Jy\,beam^{-1}km\,s^{-1}}$. **f** Velocity integrated map (from 9.4 to $36.7\,\mathrm{km\,s^{-1}}$) of the CN($N = 1 \rightarrow 0$) line emission. The contours range from -1.2 to 2.8 by $0.2\,\mathrm{Jy\,beam^{-1}km\,s^{-1}}$, and the peak value is $2.8\,\mathrm{Jy\,beam^{-1}km\,s^{-1}}$. **g-h** Interferometer HCN($J = 1 \rightarrow 0$) and CN($N = 1 \rightarrow 0$) spectra at the map centre ($\Delta v \approx 2.1\,\mathrm{km\,s^{-1}}$). **i-j** Integrated (over the maps) interferometer HCN($J = 1 \rightarrow 0$) and CN($N = 1 \rightarrow 0$) spectra ($\Delta v \approx 2.1\,\mathrm{km\,s^{-1}}$). **k** The radial brightness profiles of the HCN($1 \rightarrow 0$) (solid line) and CN($N = 1 \rightarrow 0$) (dashed line) emission close to the systemic velocity ($-16.0 \pm 2.1\,\mathrm{km\,s^{-1}}$).

points. These assumptions are based on the fact that we expect HCN to be a photospheric species, and CN to be the photodissociation product of HCN (e.g., Huggins & Glassgold 1982).

The radiation from the central source will excite the circumstellar molecules through various vibrational transitions. We have taken this into consideration by including those vibrational states regarded to be important. In addition, both HCN and CN have a hyperfine structure, and the resulting line overlaps are taken into account within the Monte Carlo scheme [see Schöier (2000) for details]. As a result the number of energy levels, and the transitions between them, will be very large. In combination with the high optical depths present in the HCN modelling some models become very time consuming.

In the case of HCN radiative excitation is primarily possible in the stretching modes at 3 μm and 5 μm and in the bending mode at 14 μm. The 5 μm transitions are about 300 times weaker than the 3 μm and 14 μm transitions (Bieging et al. 1984), and they are therefore not included in our excitation analysis. In each of the vibrational levels of HCN and $H^{13}CN$ we used rotational levels up to $J_{\max}$=20. The energy levels and radiative

rates where calculated using results in Bieging et al. (1984). We used the rotational collisional rate coefficients between HCN and He from Green & Thaddeus (1974), modified to account for the difference in molecular weights between He and H_2, and extrapolated for $J>7$ and temperatures higher than 100 K. The hyperfine structure was calculated using the results in Truong-Bach & Nguyen-Q-Rieu (1989). In the modelling, the hyperfine structure was included only for levels $J<6$ in order to limit the number of transitions in the molecular excitation analysis. The splitting of the levels become less important the higher the J-level, and this justifies a treatment of the high J rotational levels as single. Also the l-type doubling in the upper states of the 14 μm transitions was included.

For CN we include 10 rotational levels ($N_{\max}$=9), including hyperfine structure, in each of the ground state and the first excited vibrational state, which lies 4.8 μm above the ground state. We have not investigated the effect of a, potentially important, low lying electronic state of CN. The energy levels and the radiative rates are calculated using the scheme presented in Truong-Bach et al. (1987). Since the rotational collisional rates of CN are unknown we use the ones for CO, modified by the difference in molecular weights. These collisional rates were modified in order to account for the hyperfine structure following Truong-Bach et al. (1987).

In our models the v=1 levels are only radiatively excited from the ground state. Collisional excitation may become important in regions with high density and temperature, i.e., in the inner parts of CSEs. However, assuming that the unknown ro-vibrational collisional rate coefficients are not larger than those of pure rotational transition (which is reasonable here), we find in our excitation analysis that, at least in the circumstellar models presented here, vibrational excitation by collisions is unimportant when compared to radiative excitation.

Table 2. HCN modeling results compared to single dish observations.

Source	Tel.	Trans.	$I_{\rm obs}$ (K km s^{-1})	$I_{\rm mod}$ (%)	Ref.
W Ori	SEST	1−0	4.8	−76	1
	OSO	1−0	4.6	−54	1
	SEST	3−2	9.0	+11	2
	SEST	4−3	5.9	+121	2
CW Leo	NRAO	1−0	84.0	+46	3
	SEST	1−0	190.0	−11	1
	OSO	1−0	290.6	−5	1
	NRAO	3−2	547.7	+27	2
	SEST	3−2	675.9	+19	2
	JCMT	3−2	825.9	+9	3
	JCMT	4−3	1295.9	−22	3
	OSO	1−0, 13	121.9	+26	1
	JCMT	3−2, 13	419.8	+9	3
	JCMT	4−3, 13	503.2	+11	3
RW LMi	NRAO	1−0	9.2	−41	2
	SEST	1−0	22.4	−64	1
	OSO	1−0	29.7	−51	1
	NRAO	3−2	48.7	−9	2
	SEST	3−2	61.1	+4	1
	JCMT	3−2	67.7	+14	3
	OSO	1−0, 13	5.0	+10	1
Y CVn	NRAO	1−0	3.1	−63	2
	OSO	1−0	9.4	−68	1
	NRAO	3−2	9.6	+4	2
	SEST	1−0, 13	1.2	−48	2
	OSO	1−0, 13	3.3	−62	1
LP And	OSO	1−0	11.0	−10	2
	NRAO	3−2	24.1	+13	2
	OSO	1−0, 13	4.5	−4	2

1. Olofsson et al. 1993b; 2. Schöier & Olofsson (2000c, in prep.); 3. JCMT public archive.

5. Modelling of the HCN and CN emission

5.1. Observational constraints

The brightness distribution maps of the molecular line emissions, presented in Sect. 3, were used to derive radial brightness distributions, which we compared to the results of the modelling. When producing the radial brightness distributions we average the emission over a velocity interval equal to the expansion velocity of the envelope and centered on the stellar velocity. This will assure that we always have good signal-to-noise ratios. In the case of W Ori and Y CVn reliable size estimates of the HCN envelopes are not possible to obtain from our observations since the sources are not resolved. In these two cases we instead used, as conservative upper limits, envelope radii equal to one fourth of the full half power beamwidth. The derived abundances from the radiative transfer analysis will then be lower limits. For W Ori, where no CN interferometer data exist, we used the ratio of the HCN envelope size to the peak CN abundance radius from a simple chemical model (see Sect. 5.4) to estimate the peak CN radius. In addition, for W Ori and Y CVn we also constrained the width of the CN shell used in the circumstellar model, Δr, from the simple chemical model. We also produced model spectra, which would be obtained towards the centres of the CSEs with a Gaussian beam of the size of the clean beam, which were compared with the interferometer spectra towards the centre pixel.

When modelling the HCN and CN emission we have, as a complement to the interferometer data, used single dish data of various origins as further constraints (see Tables 2 & 3). These consist of mainly low transition HCN and CN data from Olofsson et al. (1993a), supplemented with new observations aimed at getting data on the higher transitions (Schöier & Olofsson 2000c, in prep.). There is some overlap between the two data sets so the quoted intensities for the Olofsson et al. (1993a) reference may differ from what was published in that paper. In addition, we have obtained HCN data from the JCMT public archive for CW Leo.

5.2. The CW Leo results

The archetypical carbon star CW Leo has been extensively studied using various molecules, among them HCN and CN. Dayal & Bieging (1995) presented an analysis of their obser-

Table 3. CN modeling results compared to single dish observations.

Source	Tel.	Trans.	$I_{\rm obs}^{\rm high}$ (K km s^{-1})	$I_{\rm obs}^{\rm low}$ (K km s^{-1})	$I_{\rm mod}^{\rm high}$ (%)	$I_{\rm mod}^{\rm low}$ (%)	$I_{\rm mod}^{\rm tot}$ (%)	Ref.
W Ori[a]	SEST	1−0	<1.0	<1.0	−	−	−	1
	OSO	1−0	<3.6	<3.6	−	−	−	2
	SEST	2−1	1.3	0.9	+23	−11	+9	2
CW Leo	NRAO	1−0	84.3	57.2	−3	−1	−2	2
	SEST	1−0	138.6	80.1	−23	−8	−17	1
	OSO	1−0	145.3	93.1	−6	+1	−3	2
	NRAO	2−1	80.3	46.9	−6	−3	−5	2
	SEST	2−1	61.1	37.5	+31	+30	+31	2
RW LMi	NRAO	1−0	12.0	7.6	−21	−13	−18	2
	SEST	1−0	24.6	16.8	−41	−40	−41	1
	OSO	1−0	39.0	23.6	−37	−29	−34	2
	NRAO	2−1	13.3	9.4	+50	+10	+33	2
	SEST	2−1	22.7	13.7	+15	0	+10	2
Y CVn	OSO	1−0	8.5	7.3	+11	−40	−13	1
	NRAO	2−1	5.3	5.5	+38	−20	0	2
LP And	OSO	1−0	11.2	6.6	−7	+2	−5	2
	NRAO	2−1	7.2	3.6	+7	0	+3	2

[a] For W Ori we derive CN($N = 1 \rightarrow 0$) model intensities (for the high and low frequency components) of 0.5 and 0.3 K kms^{-1}, and 1.0 and 0.6 K kms^{-1}, for SEST and OSO, respectively.
1. Olofsson et al. 1993; 2. Schöier & Olofsson (2000c, in prep.).

vations of HCN and CN line emission towards CW Leo using the BIMA interferometer. The excitation analysis they used was based on the Sobolev approximation. In order to estimate the HCN abundance they instead modelled the observed H^{13}CN line emission, where optical depth effects are small. They included hyperfine structure only in the lowest rotational transition, but during the excitation calculation these levels were assumed to be populated in LTE. Subsequently, departure coefficients from LTE, $b_i = n_i/n_{\rm LTE}$, were introduced for each of the three hyperfine levels i in the J=1 state, and these were then used as free parameters, which were varied until a good fit to the observed spectrum was obtained. Using this model they derived f_0(H^{13}CN)=7.8×10^{-7} and $r_{\rm e}$=2.4×10^{16} cm, assuming a distance of 100 pc and $\dot{M}$=2×10^{-5} M$_\odot$ yr^{-1}. Applying the same approch to model the H^{12}CN emission resulted in H^{12}CN/H^{13}CN abundance ratios that were much too low compared to what is obtained from observations of optically thin lines of other ^{12}C and ^{13}C-species. This illustrates that optical depth effects are important, and that the IR pumping lines are not treated correctly within the Sobolev approximation.

Dayal & Bieging (1995) did not solve the full radiative transfer for CN. Instead they used a simple LTE approach by assuming an excitation temperature of 8 K and again introduced departure coefficients from LTE. They derived $f_{\rm p}$=3.9×10^{-6}, $r_{\rm p}$=2.8×10^{16} cm, and Δr=2.4×10^{16} cm.

We have modelled the same data set as presented in Dayal & Bieging (1995) using our radiative transfer code with a detailed treatment of the hyperfine structure and overlapping lines, and with the basic parameters for the CSE as given in Table 1 and shown in Fig. 7. We have included the single dish data presented in Tables 2 & 3 as further constraints. The resulting intensities are consistent with the observations, except for the HCN($J = 1 \rightarrow 0$) line emission observed with the NRAO 12 m telescope, see Tables 2 & 3. The modelling of the interferometer data is presented in Fig. 6. Here both the calculated radial brightness distributions and the spectra at the centre position are compared with the observations. The model reproduces well both the radial distributions and the observed intensities of the various hyperfine components.

From our excitation analysis we estimate f_0(H^{13}CN)=1×10^{-6} and $r_{\rm e}$=4×10^{16} cm. Thus, in our modelling of CW Leo we get an H^{13}CN envelope with a somewhat lower abundance and a larger spatial extent compared to what was reported in Dayal & Bieging (1995), if we correct for the differences in mass loss rate and distance. This differences are most likely due to the difference in the treatment of the radiative transfer. We are also able to model the H^{12}CN emission and obtain a H^{12}CN/H^{13}CN abundace ratio of 50, i.e., the same as the ^{12}CO/^{13}CO-ratio (Schöier & Olofsson 2000a), and in good agreement with the value of ≈45 that has been obtained from observations of optically thin lines (e.g., Kahane et al. 1988). However, in order to obtain the observed interferometer flux in the H^{12}CN($J = 1 \rightarrow 0$) line at the centre position we are forced to reduce the amount of IR-flux from the central source by an order of magnitude. We will discuss this further in Sect. 5.3.

The CN modelling results in $f_{\rm p}$=8×10^{-6}, $r_{\rm p}$=5×10^{16} cm, and Δr=4×10^{16} cm. This is a slightly larger and broader CN envelope than obtained by Dayal & Bieging (1995). Again, as in the case of the HCN modelling, this is most probably reflecting the differences in the treatment of the radiative transfer. We get excitation temperatures of ≈4 to 8 K depending on the

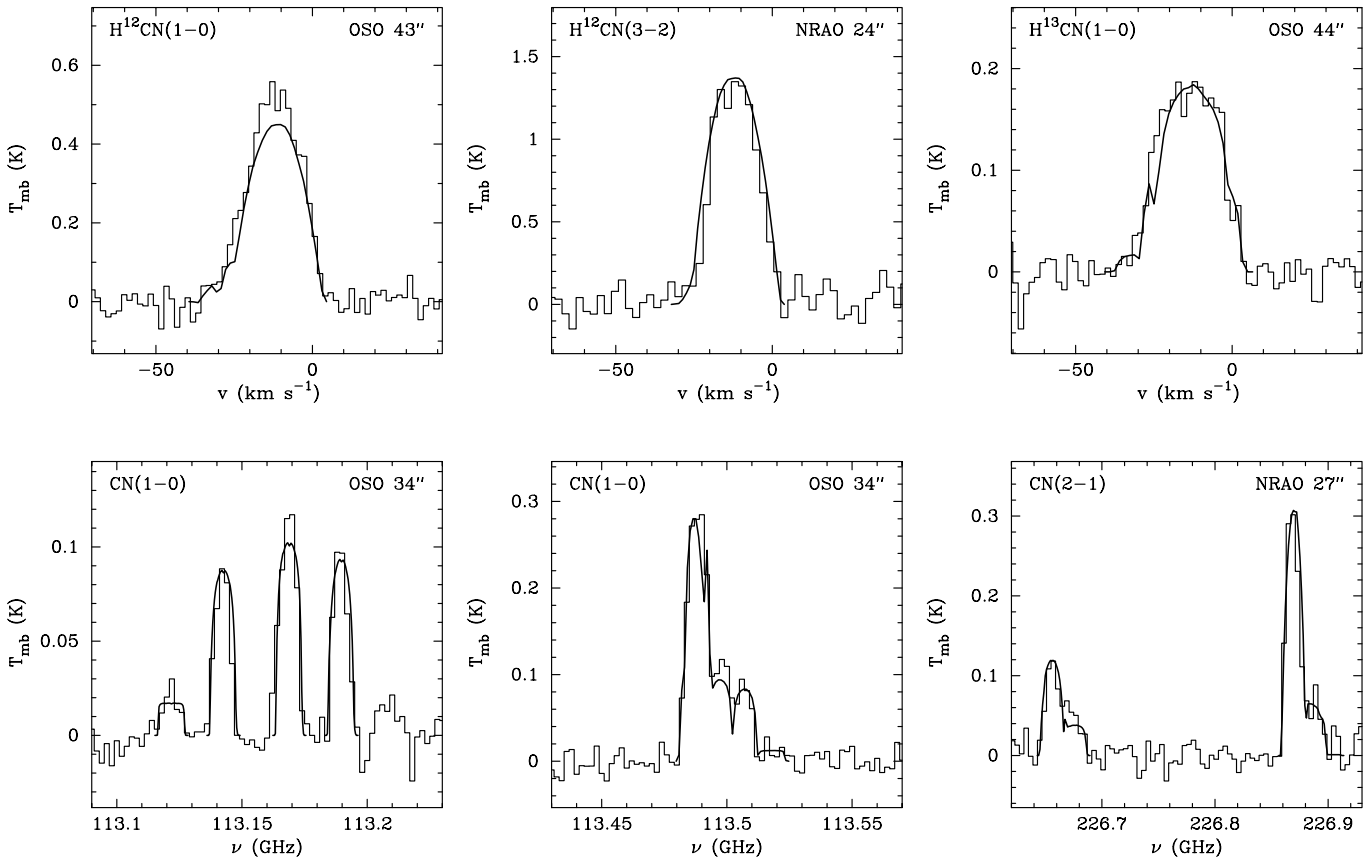

Fig. 5. Multi-transition HCN and CN spectra (histogram) observed towards LP And, overlayed with the best model results (full line) using a mass loss rate of 1.5×10^{-5} $M_\odot$ yr^{-1}, a peak HCN abundance of 3×10^{-5}, a peak CN abundance of 5×10^{-6}, and a $H^{12}CN/H^{13}CN$-ratio of 55. The telescope used, and the corresponding beamsize, for each observation is given.

hyperfine line. The results are compared with the interferometer data in Fig. 6. For CN, the total integrated intensity of the high-frequency hyperfine group of CN($N = 1 \rightarrow 0$) was used to produce the radial brightness distribution.

When producing the CN radial brightness distributions we, as did Dayal & Bieging (1995), used the high-frequency hyperfine group of the CN($N = 1 \rightarrow 0$) transition. In our models we note that the brightness distribution produced by this group, where considerable line overlap occurs, is significantly smaller in spatial extent than those of the non–overlapping lines in the low-frequency group. Recently, Lucas & Guelin (1999) presented a PdB interferometer brightness map, using the three strongest components in the low-frequency hyperfine group. This, geometrically thin, brightness distribution peaks at roughly 20″, i.e. well outside the peak radius found by Dayal & Bieging (1995) using the high-frequency group. In our model we are able to consistently model both these data sets, and to ascribe the different molecular extents to the difference in their excitation.

We have found that radiative excitation is important also for CN. Turning off the central radiation field produces CN line intensities that are significantly lower by about factor of two to three (depending on the transition). This decrease in intensity can be partly offset by increasing the CN abundance, but the overall fit to many lines is getting worse the higher the CN abundance.

Bachiller et al. (1997) also studied the CN emission towards CW Leo. Using a simple model, assuming $T_{\rm rot}$=6 K, they arrived at $f_{\rm p}$=6.2×10^{-7} with an estimated (from a simple photodissociation model) envelope extending from 1.0×10^{16} cm to 3.3×10^{16} cm. The derived CN abundance is significantly lower than our estimate. The CN envelope is smaller and located closer to the star than in our model.

5.3. Results for the other stars

The single dish observations which are used to constrain the models and the model results are presented in Tables 2 & 3. Here the observed intensities (in main beam brightness temperature scale and integrated over the line), $I_{\rm obs}$, are compared to the predicted intensities, $I_{\rm mod}$. The latter are expressed relative to the former. The fits, both to the integrated intensities as well as the overall line shapes, are generally very good, as can be seen in Fig. 5 for one of the sample stars, LP And. The fact that we are able to reproduce the observed $H^{13}CN(J = 1 \rightarrow 0)$ line emission [note that this line has a much lower optical depth than the corresponding $H^{12}CN$ line and possible numerical difficulties connected with high optical depths (e.g., convergence) are much

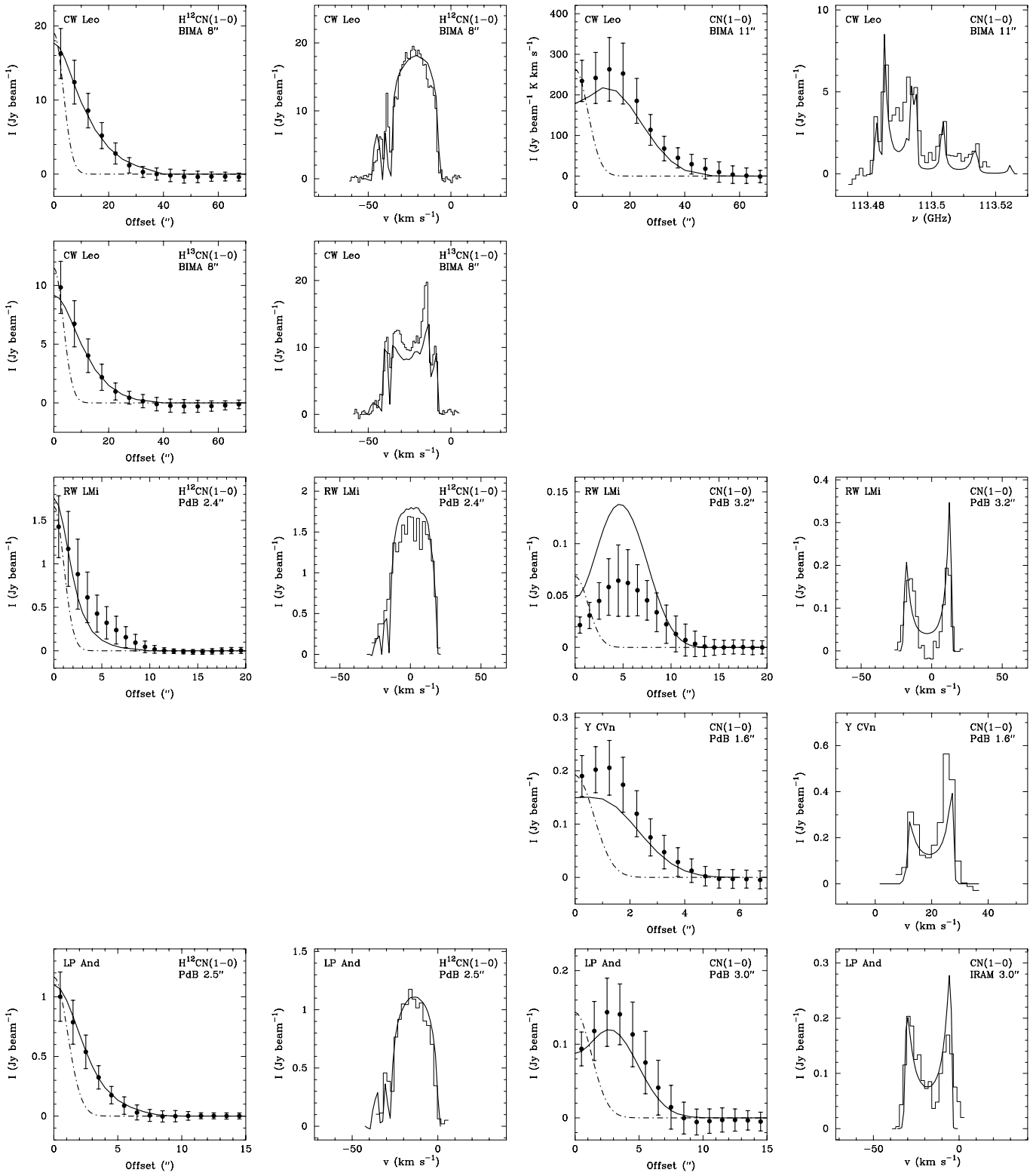

Fig. 6. Interferometer radial brightness distributions and centre spectra overlayed with the model results [full lines; note that the CN results for RW LMi, Y CVn, and LP And are obtained for an average of the three strongest hyperfine lines in the low-frequency hyperfine group of the $\mathrm{CN}(N = 1 \rightarrow 0)$ transition]. In the radial brightness distribution plots the dot–dashed line represents the circular beam (with the same surface area as the CLEAN beam) used in the radiative transfer calculations. The errors indicated in the radial plots are the quadratic sum of the statistical errors from the averaging over concentric annuli and an estimated calibration error of $\pm 20\%$.

reduced in this case] using an $H^{12}CN/H^{13}CN$–ratio equal to the $^{12}CO/^{13}CO$–ratio derived by Schöier & Olofsson (2000a) gives support to the reliability of the derived $H^{12}CN$ abundance.

The interferometer observations are compared with the model results in Fig. 6. Here both the averaged radial brightness distributions as well as the spectra obtained at the stellar positions are compared to those obtained from the models. For CN, the three strongest components in the low-frequency hyperfine group of the CN($N = 1 \rightarrow 0$) line have been averaged toghether. For LP And we are able to reproduce both the radial brightness distribution and the observed centre spectra, within the observational uncertainties, for both the HCN and CN emissions. However, when modelling the $H^{12}CN$ line emission towards this high mass loss rate object we were forced to reduce the amount of IR emission from the central star in order to reproduce the observed interferometer spectra in the inner parts of the envelope. The emission from the central star excites the ground state via pumping through mainly the 14 μm vibrational state. The effect of this pumping is that the $J = 1 \rightarrow 0$ transition becomes sub-thermally populated in the inner parts of the envelope thereby reducing the intensity emanating from this region. The same problem occurs for CW Leo (see above) and RW LMi (see below). This reflects our crude treatment of the source of IR-emission, and our lack of knowledge of the density structure and the kinematics in the inner region of the CSE. A detailed model of radiatively excited molecules would have to include this, as well as the radiative transfer in the dust present around the high mass loss rate objects.

For RW LMi we have a problem to consistently reproduce simultaneously the HCN($J = 1 \rightarrow 0$) and HCN($J = 3 \rightarrow 2$) single-dish intensities. Furthermore, if we use the estimated $^{12}CO/^{13}CO$–ratio of 35 (Schöier & Olofsson 2000a) to further constrain the model, we find that the $H^{12}CN$($J = 1 \rightarrow 0$) line is much too weak [if we reproduce the $H^{13}CN$($J = 1 \rightarrow 0$) emission which is considerably less affected by optical depth effects]. This is due to the fact that the $H^{12}CN$($J = 1 \rightarrow 0$) line is sub-thermally excited throughout the envelope. We must also decrease the luminosity of the central source by a factor of ten in order to reproduce the interferometer HCN($J = 1 \rightarrow 0$) intensities. In addition, we are not able to reproduce the observed radial HCN brightness distribution. In this connection, we mention once again the problem in modelling also the circumstellar CO emission (Schöier & Olofsson 2000b) of RW LMi.

Comparing the calculated single–dish intensities with the observed values we find that we generally have a problem with the HCN($J = 1 \rightarrow 0$) intensities for the low mass loss rate stars W Ori and Y CVn. For both objects the HCN($J = 1 \rightarrow 0$) line is known to exhibit maser features (Olofsson el al. 1993b; Izumiura et al. 1995). Although we get inversion of this line (almost throughout the entire envelope) in our model the effect is too low to explain the observed emission (see Table 2). One way to get stronger maser emission would be the introduction of high density clumps. In future improvements of the code this possibility has to be investigated. Another possibility to increase the flux in the HCN($J = 1 \rightarrow 0$) line is to significantly increase the amount of HCN present in the wind. This will, however, produce much stronger HCN($J = 3 \rightarrow 2$) line emission than what is observed. For Y CVn the HCN($J = 3 \rightarrow 2$) line is only inverted over a small part of the envelope, located close to the star, and the emission from this region does not contribute to the intensity of the single–dish model spectra [in W Ori the HCN($J = 3 \rightarrow 2$) line is not inverted at all]. In addition, there exist no observational evidence of maser emission from this transition in this type of stars. In our modelling we therefore used the observed HCN($J = 3 \rightarrow 2$) emission when estimating the HCN abundance in the low mass loss rate objects, since we believe it to be more reliable than the highly masing HCN($J = 1 \rightarrow 0$) emission. Also some of the lines in the low frequency hyperfine group of CN($N = 1 \rightarrow 0$) are inverted for the low mass loss rate stars, due to IR-pumping trough the first vibrational state. However, this CN maser is not strong and we also find that the predicted flux in the model is reasonable (see Table 3). Furthermore, we can explain the CN($N = 2 \rightarrow 1$) line intensities without having population inversion in this transition for any of the sample stars, contrary to what was suggested by Bachiller et al. (1997).

The derived molecular envelope sizes and abundances (rounded off to one significant digit) of HCN and CN are summarized in Table 4, and the abundance distributions are shown in Fig. 7. Although the estimated sizes of the HCN envelopes span over an order of magnitude the derived HCN abundances are fairly similar, around $\approx 5 \times 10^{-5}$. Olofsson et al. (1993b) estimated the photospheric HCN abundance for a large sample of optically bright carbon stars and found a value of $(2.5 \pm 1.5) \times 10^{-5}$. Thus, our results are fully consistent with a photospheric origin of HCN. For CN, there is a larger spread in the derived circumstellar abundances. However, comparing our estimates for CN with the photospheric abundances from Olofsson et al. (1993b), we note that the circumstellar value is about three orders of magnitude larger, clearly showing that CN is produced in the envelope.

Bachiller et al. (1997) have also modelled the CN emission towards our sample stars. Using a simple model assuming a constant $T_{\rm rot}$ they estimated circumstellar abundances that are in fair agreement with those derived from our modelling for W Ori, Y CVn, and LP And, but significantly lower than our estimates for RW LMi and CW Leo.

5.4. Comparison with theoretical models

Chemical models of carbon stars predict that HCN is a molecule of photospheric origin that gets photodissociated by the ambient UV–field, when the HCN envelope gets thin enough, into CN (e.g., Huggins & Glassgold 1982). The observational consequence of this is the creation of a ring of CN molecules surrounding the HCN envelope.

Using the mass loss rates and expansion velocities listed in Table 1 we have estimated various parameters of the HCN and CN envelopes from a simple photodissociation model (Huggins & Glassgold 1982). In this model the dust shielding distance (Jura & Morris 1981)

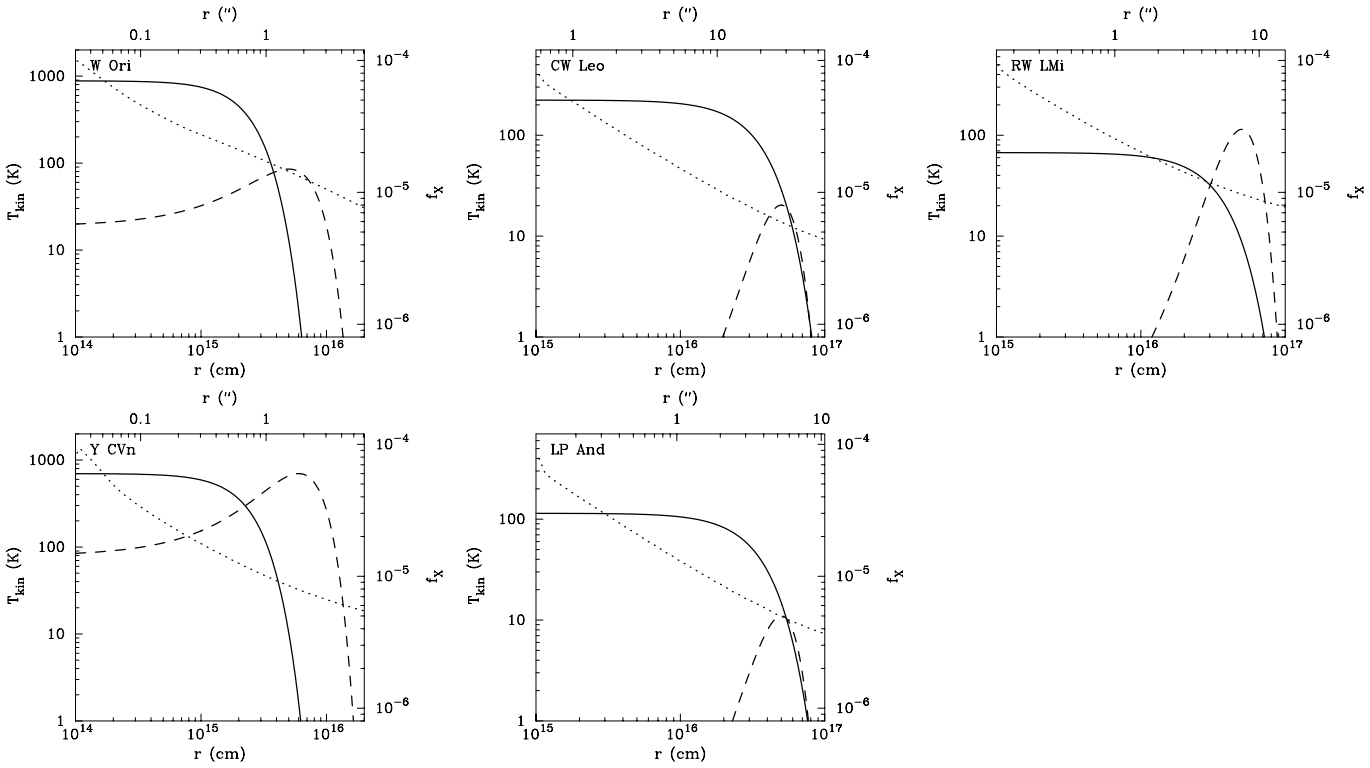

Fig. 7. The radial abundance distributions of HCN (solid) and CN (dashed) relative to H_2 for the sample stars, as derived from our circumstellar models. Also shown for each object is the kinetic temperature structure (dotted) obtained from modelling of the CO emission (Schöier & Olofsson 2000b).

Table 4. HCN and CN model parameters. A colon (:) indicates that the result from a simple chemical model has been used in order to constrain the parameter (see text for details).

Source	HCN		CN		
	f_0	r_e (cm)	f_P	r_P (cm)	Δr (cm)
W Ori	$>7\times10^{-5}$	$<3\times10^{15}$	$>1.5\times10^{-5}$	$<6\times10^{15}$:	1×10^{16}:
CW Leo	5×10^{-5}	4×10^{16}	8×10^{-6}	5×10^{16}	4×10^{16}
RW LMi	2×10^{-5}	4×10^{16}	3×10^{-5}	5×10^{16}	4×10^{16}
Y CVn	$>6\times10^{-5}$	$<3\times10^{15}$	6×10^{-5}	6×10^{15}	1×10^{16}:
LP And	3×10^{-5}	4×10^{16}	5×10^{-6}	5×10^{16}	4×10^{16}

$$d_X = 1.4\frac{3(Q/a)_X}{4\rho_d}\frac{\Psi\dot{M}}{4\pi v_d} \quad (5)$$

determines how effectively the molecules are shielded from the ambient UV–field by the dust. Here Q is the dust absorption efficiency, ρ_d is the density of a dust grain, and a is its size. Since different species are photodissociated at different wavelengths, Q/a will depend on the species under study. Here we have adopted ρ_d=2 g cm^{-3}, $(Q/a)_{HCN}$=2×10^5 cm^{-1} (Koike et al. 1980), and $(Q/a)_{CN}$=1.2×$(Q/a)_{HCN}$ (Truong-Bach et al. 1987). In Eq. (5) we have introduced the dust–to–gas ratio, Ψ. Here we adopt a value of Ψ=0.005 for all sample stars. Furthermore, the dust expansion velocity v_d was set equal to the gas expansion velocity for the high mass loss rate objects. For the low mass loss rate objects, however, we adopted a dust expansion velocity twice as large as that of the gas (cf. Olofsson et al. 1993b). In the photodissociation model we also used the unshielded photodissociation rates from van Dishoeck (1988); $G_{0,HCN}$=1.1×10^{-9} s^{-1}, and $G_{0,CN}$=2.5×10^{-10} s^{-1}.

We find that the envelope sizes (using our limited sample) should scale roughly as $(\dot{M}/v_e)^{0.6}$ for HCN and as $(\dot{M}/v_e)^{0.5}$ for CN. The CN to HCN abundance ratio should be ≈0.7, with only a weak mass loss rate dependance. Our results are qualitatively consistent with such a picture, Fig. 8. Our modelling of the observations results in HCN envelope sizes, r_e, which scale roughly as $(\dot{M}/v_e)^{0.7}$, i.e., in good agreement with the prediction from the photodissociation model, Fig. 8a. The estimated CN envelope sizes, r_p, scale roughly as $(\dot{M}/v_e)^{0.5}$, in excellent agreement with the model prediction, Fig. 8b. While we find the expected behaviour with respect to the thickness of the molecular envelopes, $(\dot{M}/v_e)$, their sizes are larger, on the average, by

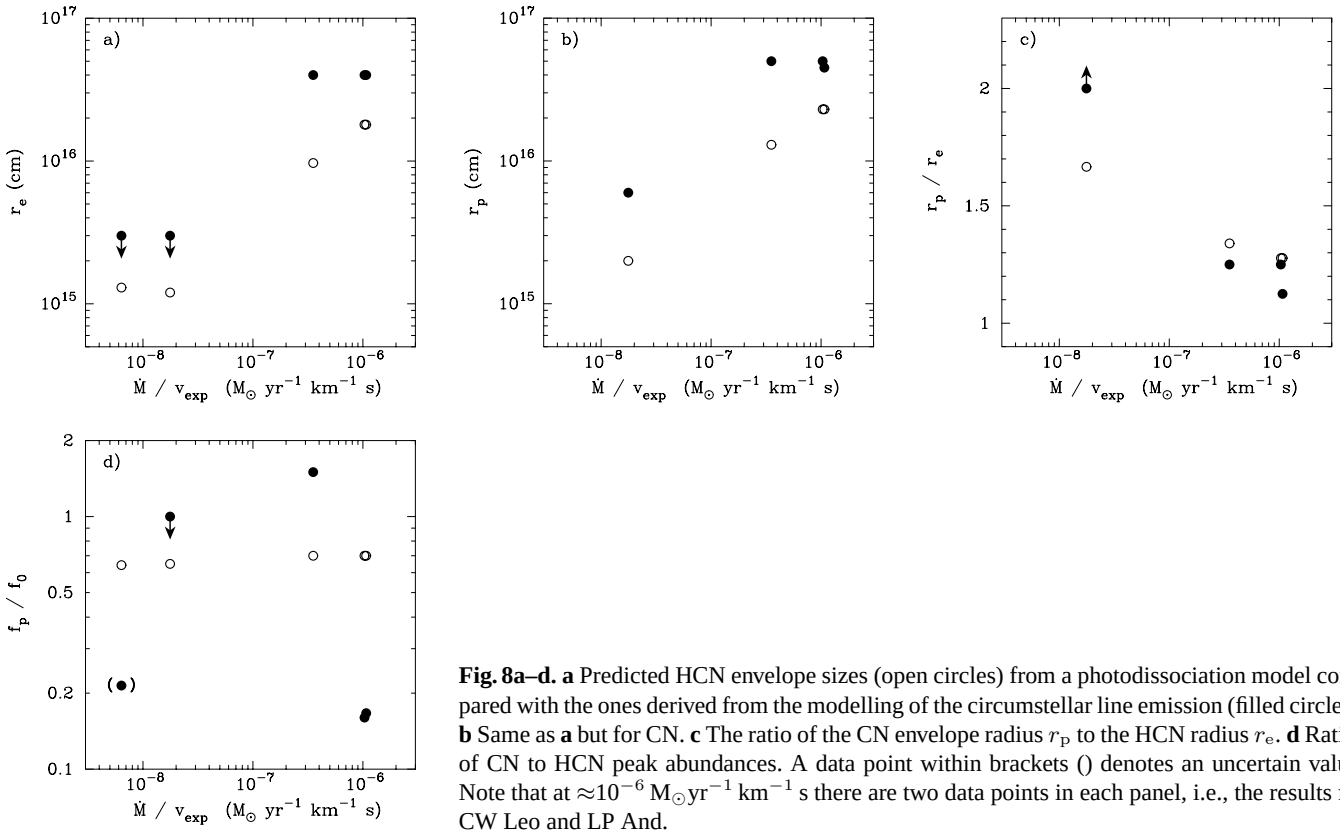

Fig. 8a–d. a Predicted HCN envelope sizes (open circles) from a photodissociation model compared with the ones derived from the modelling of the circumstellar line emission (filled circles). **b** Same as **a** but for CN. **c** The ratio of the CN envelope radius $r_{\rm p}$ to the HCN radius $r_{\rm e}$. **d** Ratios of CN to HCN peak abundances. A data point within brackets () denotes an uncertain value. Note that at $\approx 10^{-6}$ $M_\odot$yr^{-1} km^{-1} s there are two data points in each panel, i.e., the results for CW Leo and LP And.

about a factor of two than what is predicted by the photodissociation model. It should be noted, however, that some of the input parameters to the photodissociation model are highly uncertain. One should also keep in mind that we have used simple Gaussians to represent the abundance distributions in the circumstellar model. Based on tests we estimate that "observed" $r_{\rm e}$ and $r_{\rm p}$ will be somewhat smaller if we use the radial dependence of the abundance distributions that come out of the photodissociation model.

The ratio of the CN to HCN molecular envelope sizes, $r_{\rm p}/r_{\rm e}$, are above unity for all stars supporting the prediction from the photodissociation models that the CN emitting region should reside outside that of HCN, Fig. 8c. Observationally this ratio has a somewhat stronger mass loss rate dependence than what is expected. In Fig. 8d we compare the CN to HCN peak abundances, $f_{\rm p}/f_0$.

It is clear that the abundances have the largest uncertainties of the estimated quantities, and it is also difficult to see a definite trend in the results for the CN/HCN peak abundance ratio. The most reliable results are probably those for the high mass loss rate objects. For (LP And and CW Leo) we find $f_{\rm p}/f_0 \approx 0.16$ [we note that Dayal & Bieging (1995) derived a value of 0.12 for CW Leo], significantly lower than what is predicted in the simple photodissociation model. Such low values can only be obtained in this model if the photodissociation rate of CN is significantly higher, relative to that of HCN, than what we have used. Another possible explanation would be a chemical reaction which destroys CN, and that has not been included in the more elaborate chemical models by e.g. Cherchneff et al. (1993). Dayal & Bieging (1995) discuss this, but reach no definite conclusion. It is important to get better interferometer data on lower mass loss rate objects to identify any possible trend, which may shed light on this problem. The result for RW LMi is peculiar in the sense that the derived CN abundance is larger than the HCN abundance. However, RW LMi appears to have a strange envelope, and the derived CN to HCN abundance ratio may be an artifact of the inability of our assumed model to represent this CSE.

6. Other emissions towards RW LMi

In this section we present other emissions obtained towards RW LMi. They where all obtained simultaneously. Due to the complicated nature of some of the emissions, and the problems we have experienced in modelling the CO, HCN and CN data of RW LMi, we have chosen not to present a model for these data. We discuss the detection of continuum emission, and the SiS($J = 5 \rightarrow 4$), HC_3N($J = 10 \rightarrow 9$), HC_5N($J = 34 \rightarrow 33$) and HNC($J = 1 \rightarrow 0$) line emissions. It should be noted that for these data we have a full synthesis observation. Finally, we discuss the result that the position of the peak intensity changes systematically across the line profile for some of the emissions.

6.1. Continuum emission

We have detected continuum emission at 90.7 GHz towards RW LMi by averaging data free of line emission (the total

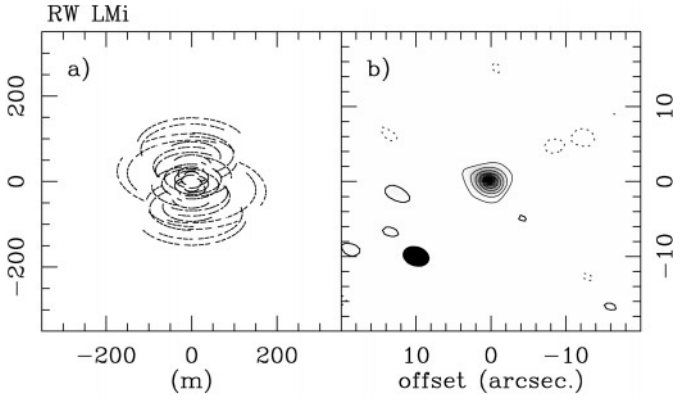

Fig. 9a and b. Continuum emission map at 90.7 GHz (within ≈400 MHz) towards RW LMi using uniform weighting. The coordinates are relative to $\alpha(J2000) = 10^{\rm h}16^{\rm m}02\overset{\rm s}{.}28$ and $\delta(J2000) = 30°34'18\overset{''}{.}9$. Contours range from -2 to 6 by $1\,\mathrm{mJy\,beam^{-1}}$, and the peak value is $6.2\,\mathrm{mJy\,beam^{-1}}$. The synthesized CLEAN beam is $3\overset{''}{.}6 \times 2\overset{''}{.}6$ with a position angle of 73°.

bandwidth used is about 400 MHz), Fig. 9. The peak intensity is $\approx 6.4\,\mathrm{mJy\,beam^{-1}}$ and the flux density is about 8 mJy. The rms in the image is about $\approx 0.4\,\mathrm{mJy\,beam^{-1}}$. We have determined the position of the peak by fitting a circular Gaussian to the data in the Fourier plane. The result is $\alpha(J2000) = 10^{\rm h}16^{\rm m}02\overset{\rm s}{.}28$ and $\delta(J2000) = 30°34'18\overset{''}{.}9$, which we have adopted as the centre position for RW LMi in the analysis of the line emission. The error obtained from the model fit is $0\overset{''}{.}1$ both in α and δ. The position is consistent, within the absolute positional uncertainty of $\leq 0\overset{''}{.}5$, with the HCN maser position found by Carlstrom et al. (1990), $\alpha(J2000) = 10^{\rm h}16^{\rm m}02\overset{\rm s}{.}29$ and $\delta(J2000) = 30°34'18\overset{''}{.}8$. It is also consistent with the best published IR position (with an uncertainty of 3″), $\alpha(J2000) = 10^{\rm h}16^{\rm m}02\overset{\rm s}{.}35$ and $\delta(J2000) = 30°34'19\overset{''}{.}0$ (Claussen et al. 1987) The estimated half-power radius, $1\overset{''}{.}6 \pm 0\overset{''}{.}4$, which corresponds to a linear size of ≈700 AU, should be considered as an upper limit. Neri et al. (1998) obtained a value of 13.3 mJy at 112 GHz towards RW LMi. In addition, RW LMi has been observed in three submillimetre bands (264, 394 and 685 GHz) by Marshall et al. (1992). Our data point at 90.7 GHz is consistent with these data and a spectral index of $S(\lambda) = \lambda^{-3.1}$.

6.2. SiS

The SiS($J = 5 \rightarrow 4$) data towards RW LMi are presented in Fig. 10a. The average half-power radius, using a Gaussian function to fit the data (in the velocity interval $-1.0 \pm 2.1\,\mathrm{km\,s^{-1}}$) in the Fourier plane, is $1\overset{''}{.}3 \pm 0\overset{''}{.}1$ ($\approx 8.6 \times 10^{15}$ cm), and the expected size dependence on the line-of-sight velocity is present. The emission in the velocity-channel maps are not resolved. The brightness peaks close to the adopted centre position and falls off rapidly as a function of the projected distance. This is qualitatively consistent with the results towards CW Leo (Bieging & Nguyen-Q-Rieu 1989; Bieging & Tafalla 1993; Lucas et al. 1995), suggesting that this molecule is of photospheric origin. The size of the SiS($J = 5 \rightarrow 4$) emitting region of RW LMi is smaller than that of CW Leo, which may be explained by the difference in mass loss rates. Lucas et al. (1995) showed that the brightness distribution of SiS($J = 5 \rightarrow 4$) towards CW Leo is a mixture of a centrally peaked source and a surrounding second envelope. This is not seen towards RW LMi, possibly due to a lack of angular resolution. Even though our data support the idea that both SiS and HCN are of photospheric origin, the angular size of SiS is considerably smaller than that of HCN as noted by Bieging & Tafalla (1993) for CW Leo. Both the integrated spectrum and the spectrum at the centre pixel are very asymmetric (triangular) with the red-shifted emission much stronger than the blue-shifted one. This is very different from the result obtained towards CW Leo, where the SiS($J = 5 \rightarrow 4$) line profile at the map centre is symmetric and has horns at the extreme velocities (Bieging & Nguyen-Q-Rieu 1989). Furthermore, we note that a line intensity ratio involving SiS is very different for the two stars (Bujarrabal et al. 1994; Olofsson et al. 1998). This may indicate more complicated excitation effects in RW LMi. We have also made maps using natural weighting, and the results are similar to those presented in Fig. 10. Since we are not resolving the emission, the radial brightness profile presented in Fig. 10k merely reflects the beam profile. The flux density in the integrated (from -24.1 to $+22.2\,\mathrm{km\,s^{-1}}$) line profile, Fig. 10i, is $\approx 16\,\mathrm{Jy\,km\,s^{-1}}$. Bujarrabal et al. (1994), using the IRAM 30 m telescope, found a flux density of $13\,\mathrm{Jy\,km\,s^{-1}}$. Thus, we may conclude that, within the measurement errors, the map contains all of the SiS($J = 5 \rightarrow 4$) emission.

6.3. HC_3N

The HC_3N($J = 10 \rightarrow 9$) data towards RW LMi are presented in Fig. 10. The average half-power radius is $4\overset{''}{.}0 \pm 0\overset{''}{.}1$ ($\approx 2.6 \times 10^{16}$ cm) using a Gaussian model to fit the data (in the velocity interval $-1.0 \pm 2.1\,\mathrm{km\,s^{-1}}$) in the Fourier plane, while a disk brightness distribution results in a radius of $5\overset{''}{.}4 \pm 0\overset{''}{.}1$ ($\approx 3.6 \times 10^{16}$ cm). The expected size dependence on the line-of-sight velocity is clearly seen. However, the brightness maps, Fig. 10d, and the radial brightness profile, Fig. 10k, suggest a mixture of normal envelope and shell emission, although we are barely resolving the emission in this case. The emission appears stronger towards the SE [as opposed to the HCN($J = 1 \rightarrow 0$) and CN($N = 1 \rightarrow 0$) emissions, which are strongest towards the NE, but in agreement with the HC_5N($J = 34 \rightarrow 33$) and HNC($J = 1 \rightarrow 0$) emissions] and open towards the W [as are the CN($N = 1 \rightarrow 0$) and HNC($J = 1 \rightarrow 0$) emissions]. As opposed to the CN($N = 1 \rightarrow 0$), and, in particular, the SiS($J = 5 \rightarrow 4$) and HNC($J = 1 \rightarrow 0$) spectra, the extreme red-shifted emission is not markedly stronger in this case, Fig. 10h. The integrated spectrum, Fig. 10j, suggests optically thin emission. The flux density of the integrated (from -24.1 to $+22.2\,\mathrm{km\,s^{-1}}$) line profile, Fig. 10j, is $\approx 97\,\mathrm{Jy\,km\,s^{-1}}$. Bujarrabal et al. (1994), using the IRAM 30 m telescope, found a flux density of $98\,\mathrm{Jy\,km\,s^{-1}}$. Thus, we may conclude that the map contains all of the HC_3N($J = 10 \rightarrow 9$) emission.

Bieging & Nguyen-Q-Rieu (1989) observed the same HC_3N transition towards CW Leo. They concluded that HC_3N

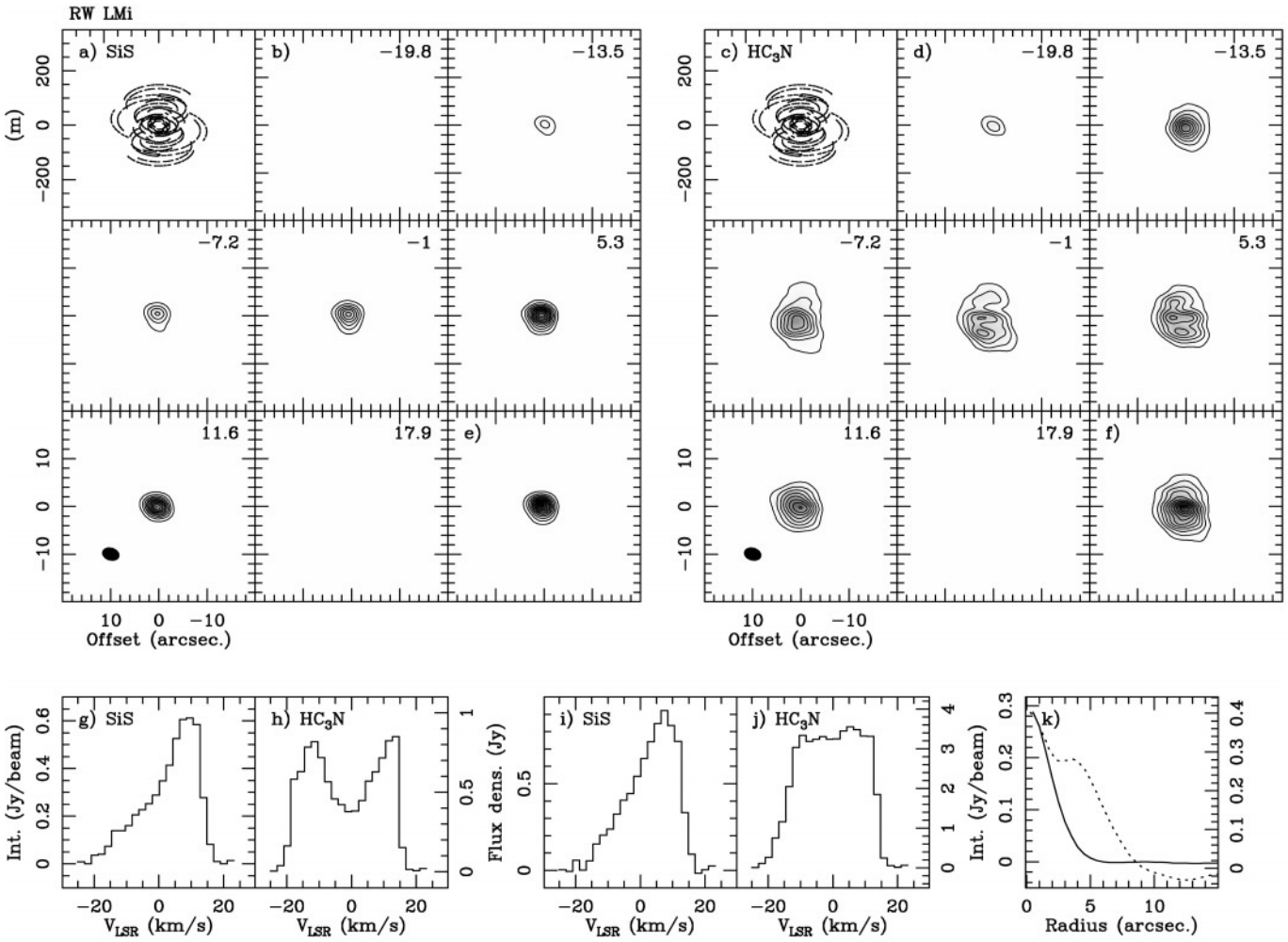

Fig. 10a–k. Results for RW LMi. **a** The UV-plane coverage for the SiS($J = 5 \rightarrow 4$) observations. **b** Velocity-channel maps ($\Delta v \approx 6.3\,\mathrm{km\,s^{-1}}$), using uniform weighting, of the SiS($J = 5 \rightarrow 4$) line emission. The pixel size is $0\farcs5 \times 0\farcs5$. The coordinates are relative to $\alpha(J2000) = 10^{\mathrm{h}}16^{\mathrm{m}}02\fs28$ and $\delta(J2000) = 30^{\circ}34'18\farcs9$. The contours range from -0.05 to 0.65 by $0.05\,\mathrm{Jy\,beam^{-1}}$. The peak value is $0.63\,\mathrm{Jy\,beam^{-1}}$, and $1.0\,\mathrm{Jy\,beam^{-1}}$ corresponds to a brightness temperature of 15.7 K. The synthesized CLEAN beam is $3\farcs6 \times 2\farcs6$ with a position angle of 73°. **c** The UV-plane coverage for the HC_3N($J = 10 \rightarrow 9$) observations. **d** Velocity-channel maps of the HC_3N($J = 10 \rightarrow 9$) line emission. The pixel size is $0\farcs3 \times 0\farcs3$. The contours range from -0.1 to 1.0 by $0.1\,\mathrm{Jy\,beam^{-1}}$. The peak value is $0.99\,\mathrm{Jy\,beam^{-1}}$, and $1.0\,\mathrm{Jy\,beam^{-1}}$ corresponds to a brightness temperature of 15.6 K. The synthesized CLEAN beam is $3\farcs6 \times 2\farcs6$ with a position angle of 73°. The rest as in Fig. 10b. **e** Velocity integrated map (from -24.1 to $22.2\,\mathrm{km\,s^{-1}}$) of the SiS($J = 5 \rightarrow 4$) line emission. The contours range from -0.5 to 5 by $0.5\,\mathrm{Jy\,beam^{-1}km\,s^{-1}}$. The peak value is $5.2\,\mathrm{Jy\,beam^{-1}km\,s^{-1}}$. **f** Velocity integrated map (from -24.1 to $22.2\,\mathrm{km\,s^{-1}}$) of the HC_3N($J = 10 \rightarrow 9$) line emission. The contours range from -1.0 to 11.0 by $1.0\,\mathrm{Jy\,beam^{-1}km\,s^{-1}}$. The peak value is $10.8\,\mathrm{Jy\,beam^{-1}km\,s^{-1}}$. **g-h** Interferometer SiS($J = 5 \rightarrow 4$) and HC_3N($J = 10 \rightarrow 9$) spectra at the map centre ($\Delta v \approx 2.1\,\mathrm{km\,s^{-1}}$). **i-j** Integrated (over the maps) interferometer SiS($J = 5 \rightarrow 4$) and HC_3N($J = 10 \rightarrow 9$) spectra ($\Delta v \approx 2.1\,\mathrm{km\,s^{-1}}$). **k** The radial brightness profiles of the SiS($J = 5 \rightarrow 4$) (solid line) and HC_3N($J = 10 \rightarrow 9$) (dashed line) emission close to the systemic velocity ($-1.0 \pm 2.1\,\mathrm{km\,s^{-1}}$).

was produced by two chemical pathways, one occurring close to the star, and one in the outer envelope. On the other hand, Bieging & Tafalla (1993), who observed the HC_3N($J = 12 \rightarrow 11$) line, showed that a non-zero abundance at the stellar position was not supported by their analysis. Our data have too low angular resolution to allow a firm conclusion about this to be drawn.

6.4. HC_5N

The HC_5N($J = 34 \rightarrow 33$) data towards RW LMi are presented in Fig. 11. The half-power radius, using a Gaussian model to fit the data (in the velocity interval $-1.0 \pm 2.1\,\mathrm{km\,s^{-1}}$) in the Fourier plane, is $4\farcs4 \pm 0\farcs9$ ($\approx 2.9 \times 10^{16}\,\mathrm{cm}$), while a disk brightness distribution results in a radius of $5\farcs9 \pm 0\farcs7$ ($\approx 3.9 \times 10^{16}\,\mathrm{cm}$). The expected size dependence on the line-of-sight velocity is clearly seen. The brightness distribution in the channel maps, as well as the centre pixel spectrum, indicate a shell distribution, but there may also be a contribution from normal envelope emission as is the case for the HC_3N($J = 10 \rightarrow 9$) emission. The emission seems to be stronger towards the SE. The integrated spectrum indicates optically thin emission. The

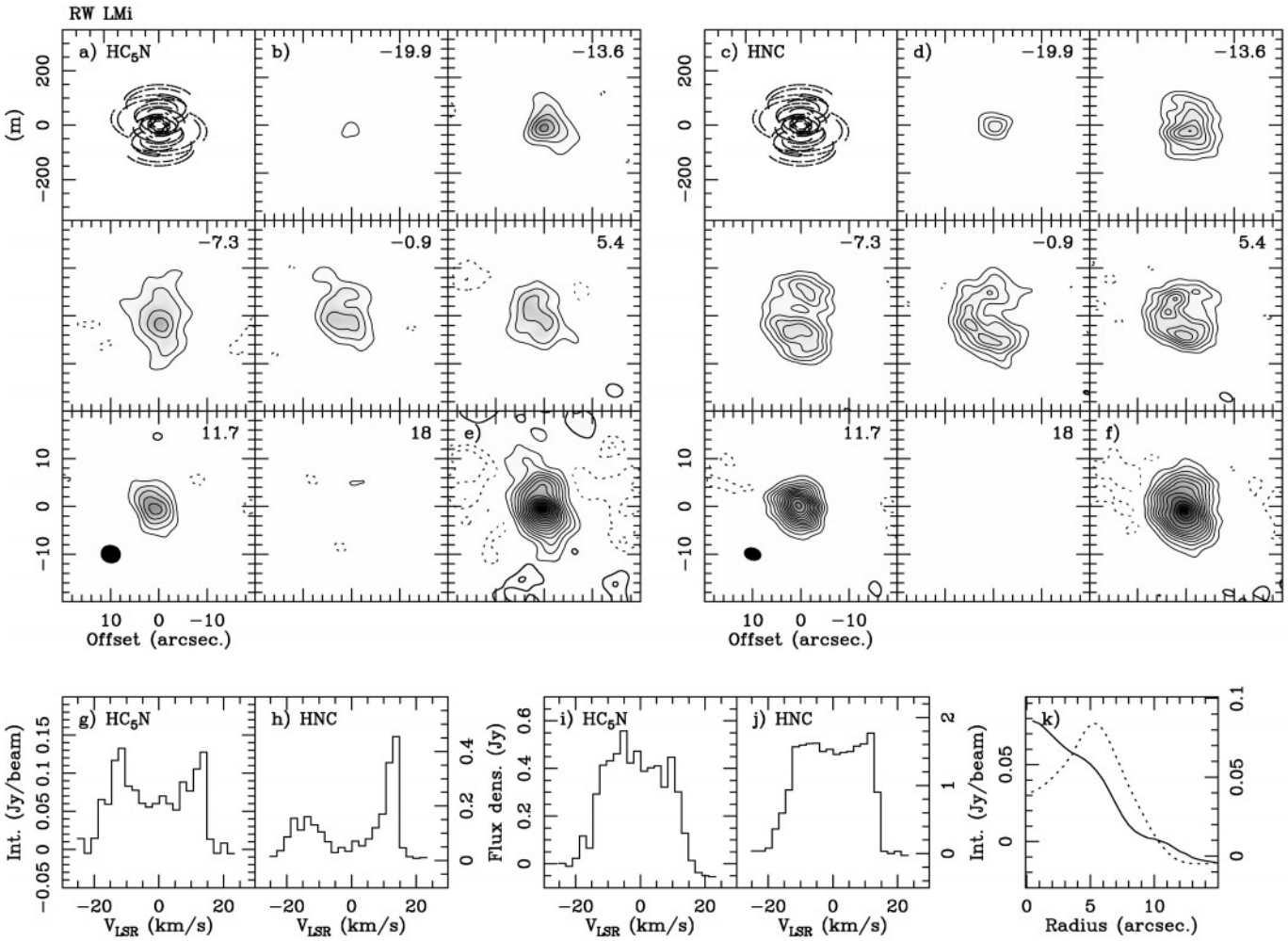

Fig. 11a–k. Results for RW LMi. **a** The UV-plane coverage for the HC_5N($J = 34 \rightarrow 33$) observations. **b** Velocity-channel maps ($\Delta v \approx 6.3\,\mathrm{km\,s^{-1}}$), using natural weighting, of the HC_5N($J = 34 \rightarrow 33$) line emission. The pixel size is $0\farcs5 \times 0\farcs5$. The coordinates are relative to $\alpha(J2000) = 10^{\mathrm{h}}16^{\mathrm{m}}02\fs28$ and $\delta(J2000) = 30^\circ34'18\farcs9$. The central LSR velocity of each channel is given in the upper right corner. The contours range from -0.06 to 0.16 by $0.02\,\mathrm{Jy\,beam^{-1}}$. The peak value is $0.16\,\mathrm{Jy\,beam^{-1}}$. $1.0\,\mathrm{Jy\,beam^{-1}}$ correspond to a brightness temperature of 9.6 K. The synthesized CLEAN beam is $4\farcs2 \times 3\farcs7$ with a position angle of 72°. **c** The UV-plane coverage for the HNC($J = 1 \rightarrow 0$) observations. **d** Velocity-channel maps, using uniform weighting, of the HNC($J = 1 \rightarrow 0$) line emission. The pixel size is $0\farcs3 \times 0\farcs3$. The contours range from -0.05 to 0.45 by $0.025\,\mathrm{Jy\,beam^{-1}}$. The peak value is $0.46\,\mathrm{Jy\,beam^{-1}}$. $1.0\,\mathrm{Jy\,beam^{-1}}$ correspond to a brightness temperature of 15.6 K. The synthesized CLEAN beam is $3\farcs6 \times 2\farcs6$ with a position angle of 72°. The rest as in Fig. 11b. **e** Velocity integrated map (from -24.1 to $22.2\,\mathrm{km\,s^{-1}}$) of the HC_5N($J = 34 \rightarrow 33$) line emission. The contours range from -0.3 to 1.4 by $0.1\,\mathrm{Jy\,beam^{-1}km\,s^{-1}}$. The peak value is $1.4\,\mathrm{Jy\,beam^{-1}km\,s^{-1}}$. **f** Velocity integrated map (from -24.1 to $22.2\,\mathrm{km\,s^{-1}}$) of the HNC($J = 1 \rightarrow 0$) line emission. The contours range from -0.4 to 2.6 by $0.2\,\mathrm{Jy\,beam^{-1}km\,s^{-1}}$. The peak value is $2.6\,\mathrm{Jy\,beam^{-1}km\,s^{-1}}$. **g-h** Interferometer HC_5N($J = 34 \rightarrow 33$) and HNC($J = 1 \rightarrow 0$) spectra at the map centre ($\Delta v \approx 2.1\,\mathrm{km\,s^{-1}}$). **i-j** Integrated (over the maps) interferometer HC_5N($J = 34 \rightarrow 33$) and HNC($J = 1 \rightarrow 0$) spectra ($\Delta v \approx 2.1\,\mathrm{km\,s^{-1}}$). **k** The radial brightness profiles of the HC_5N($J = 34 \rightarrow 33$) (solid line) and HNC($J = 1 \rightarrow 0$) (dashed line) emission close to the systemic velocity ($-1.0 \pm 2.1\,\mathrm{km\,s^{-1}}$).

centre pixel spectrum is much more symmetric than those of CN($N = 1 \rightarrow 0$), SiS($J = 5 \rightarrow 4$) and HNC($J = 1 \rightarrow 0$). The flux density of the integrated (from -24.1 to $+22.2\,\mathrm{km\,s^{-1}}$) line profile, Fig. 11f, is $\approx$12 $\mathrm{Jy\,km\,s^{-1}}$. Bujarrabal (private communication), using the IRAM 30 m telescope, found a flux density of about $14\,\mathrm{Jy\,km\,s^{-1}}$. Thus, we may conclude that the map contains all of the HC_5N($J = 34 \rightarrow 33$) emission.

Lucas & Guélin (1999) presented PdB data towards CW Leo and showed that the spatial distributions of HC_3N and HC_5N are very similar. However, in the case of RW LMi it seems that the angular size of HC_5N may be larger than that of HC_3N even though the emissions are not completely resolved. This is consistent with the results of chemical models (Cherchneff et al. 1993; Millar & Herbst 1994).

6.5. HNC

The HNC($J = 1 \rightarrow 0$) data towards RW LMi are presented in Fig. 11. The average half-power radius, using a Gaussian model to fit the data (in the velocity interval $-1.0 \pm 2.1\,\mathrm{km\,s^{-1}}$) in

the Fourier plane, is $5\farcs5 \pm 0\farcs3$ ($\approx 3.6 \times 10^{16}$ cm), while using a disk brightness distribution results in a radius of $7\farcs8 \pm 0\farcs2$ ($\approx 5.1 \times 10^{16}$ cm). The expected size dependence on the line-of-sight velocity is clearly seen. However, neither of these models represent well the true brightness distribution of the HNC($J = 1 \rightarrow 0$) line. The velocity-channel maps suggest an incomplete shell distribution. The radial brightness profile (integrated over the velocity interval -1.0 ± 2.1 km s^{-1}) indicates a shell of radius $\approx 5''$. The width of the shell may be unresolved. The brightness distribution around the systemic velocity is strongest towards the SE and open towards the W. The integrated spectrum is essentially flat, indicating that the emission is optically thin. The spectrum at the centre pixel is very asymmetric with a very strong redshifted peak [significantly more asymmetric than the CN($N = 1 \rightarrow 0$) line]. The horns at the extreme velocities is the characteristic of emission from an (at least partly) resolved shell. The flux density of the integrated (from -24.1 to $+22.2$ km s^{-1}) line profile, Fig. 11b, is $\approx$46 Jy km s^{-1}. Bujarrabal et al. (1994), using the IRAM 30 m telescope, found a flux density of 45 Jy km s^{-1}. Thus, we may conclude that the map contains all of the HNC($J = 1 \rightarrow 0$) emission.

Lucas & Guélin (1999) presented HNC($J = 1 \rightarrow 0$) data, obtained with the PdB, towards CW Leo and concluded that the emission was less extended than the CN($N = 1 \rightarrow 0$) emission, but larger than e.g. the emissions of HC_3N and HC_5N. This is also the case for our data even though the brightness distribution deviates from spherical symmetry.

6.6. Brightness peak position

For some of the emissions towards RW LMi we have found that the position of the peak brightness changes systematically across the line profile. This is particularly true for HCN($J = 1 \rightarrow 0$), HNC($J = 1 \rightarrow 0$), HC_3N($J = 10 \rightarrow 9$) and to some extent SiS($J = 5 \rightarrow 4$), Fig. 12. For CN($N = 1 \rightarrow 0$) it is difficult to obtain a reliable estimate of the position offsets around the systemic velocity due to the complicated brightness distribution, and the HC_5N($J = 34 \rightarrow 33$) emission is too weak. Fig. 12 shows the result of the fitting process, i.e., the position offsets in α and δ (arc seconds) of the model source (a circular Gaussian source) from the phase reference centre. In this case the offset is with respect to the continuum position (see above), which we have adopted as the centre position for all RW LMi data. Each emission is represented with different line styles (see upper right corner) and the points represent the position offset for the different velocity-channels starting at -15.7 km s^{-1} (this corresponds to channel 5 in our data). We have marked the velocity-channels for all emissions and all channel numbers are given for HCN (from 5 to 19). The systemic velocity occurs at channel 12 for all emissions. It is clear that there is a small offset between the position of the SiS($J = 5 \rightarrow 4$) emission, which also originates relatively closely to the star, and the continuum position. The position, at the systemic velocity, for SiS($J = 5 \rightarrow 4$) is $\alpha(J2000) = 10^{\rm h}16^{\rm m}02\fs33$ and $\delta(J2000) = 30^\circ34'19\farcs1$ compared to the adopted centre position, $\alpha(J2000) = 10^{\rm h}16^{\rm m}02\fs28$ and $\delta(J2000) = 30^\circ34'18\farcs9$. The effect is more prominent for the extended emissions. The position offsets are rather small at the extreme velocities, but increase systematically towards the systemic velocity where the offset is largest. It seems that the most reasonable explanation for this is a large-scale asymmetry in the CSE. We note that asymmetries are also seen in optical data. RW LMi has been observed with the Hubble Space Telescope and we have extracted WFPC2 images from the HST data archive. The images reveal interesting structure, e.g., the F675W filter show two objects separated by about $0\farcs25$ whereas only one object is seen in the F439W filter.

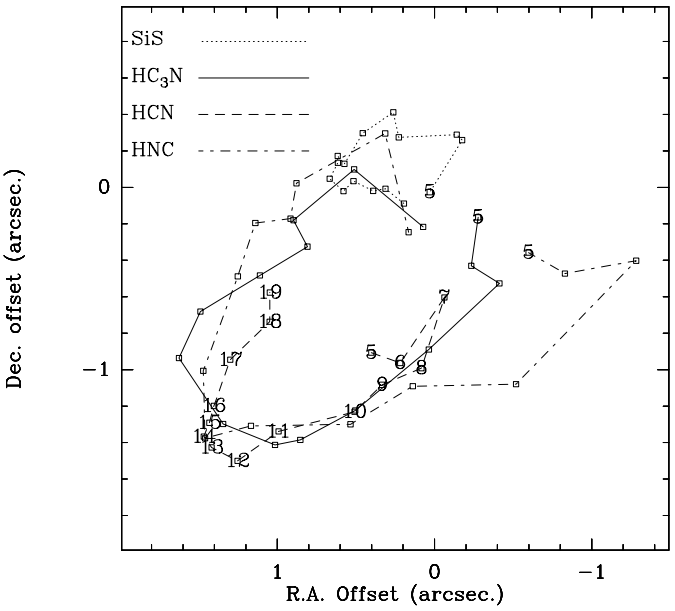

Fig. 12. The peak positions in individual channels across the line profile for different molecules observed towards RW LMi (see text for details).

7. Conclusions

We have used the IRAM interferometer on Plateau de Bure to observe four carbon stars (W Ori, RW LMi, Y CVn, and LP And) in the HCN($J = 1 \rightarrow 0$) line, and three of them (RW LMi, Y CVn, and LP And) also in the CN($N = 1 \rightarrow 0$) line. In addition, we have obtained line brightness distributions of SiS($J = 5 \rightarrow 4$), HNC($J = 1 \rightarrow 0$), HC_3N($J = 10 \rightarrow 9$), and HC_5N($J = 34 \rightarrow 33$) towards the high mass loss rate carbon star RW LMi. This sample of stars spans about two orders of magnitude in the mass loss rate. The HCN brightness distributions peak (within the errors) on the stellar positions, suggesting a photospheric origin for this molecule. The expected structure of a hollow CN brightness distribution outside that of the HCN emitting region is also seen (RW LMi and LP And), supporting theoretical models which suggest that circumstellar CN is a photodissociation product of HCN. These results are further strengthened by detailed modelling of the interferometer and multi-transition single-dish data, which gives results qualitatively, and in most cases also quantitatively, consistent with a simple photodissociation model. The

most notable discrepancy is the low CN/HCN peak abundance ratios obtained for those objects with the best observational constraints. These are lower by at least a factor of two compared to the results of also more elaborate chemical models.

We find it difficult to reproduce the observed HCN($J = 1 \rightarrow 0$) lines for the low mass loss rate objects. Even though this transition is inverted in the model, the effect is not large enough to explain the strength of the observed, apparently masing lines. For the high mass loss rate objects the interferometer HCN($J = 1 \rightarrow 0$) lines are too weak in the model. We ascribe this to a too crude treatment of the radiative excitation in the inner regions of the CSEs, and to a lack of knowledge of the density structure and kinematics in this region. The UV-coverages of our observations are limited, but it appears that the brightness distributions are genuinely patchy, suggesting a clumpy circumstellar medium.

In general, we find it difficult to fit the CO, HCN, and CN data towards RW LMi, and we suspect that this CSE departs significantly from our assumptions of spherical symmetry and/or constant mass loss rate with time. Both the HCN($J = 1 \rightarrow 0$) and CN($N = 1 \rightarrow 0$) data suggest an elongated structure with a major axis along the position angle $\approx -25^\circ$. All emissions that have a shell component are clearly weaker towards the west. The HCN($J = 1 \rightarrow 0$) and CN($N = 1 \rightarrow 0$) emissions are strongest in the north-east, while, the HNC($J = 1 \rightarrow 0$), HC_3N($J = 10 \rightarrow 9$), and HC_5N($J = 34 \rightarrow 33$) emissions are strongest towards the south-east. The peak position of the HCN($J = 1 \rightarrow 0$), HNC($J = 1 \rightarrow 0$), and HC_3N($J = 10 \rightarrow 9$) brightnesses varies systematically with the velocity, most likely an effect of a large-scale asymmetry in the CSE. The SiS($J = 5 \rightarrow 4$) emission is clearly confined to regions close to the star. The SiS($J = 5 \rightarrow 4$) and HNC($J = 1 \rightarrow 0$) line profiles [and to a lesser extent that of CN($N = 1 \rightarrow 0$)] are very asymmetric with the redshifted side being much stronger than the blueshifted side. A much more detailed study is required to understand the structure of the CSE around RW LMi.

Acknowledgements. ML acknowledges support from the U.S. National Aeronautics and Space Administration through grant NAG 5-3042 to the NICMOS Instrument Definition Team. Part of this work was done when ML was supported by an ESA external fellowship at Sterrewacht Leiden, The Netherlands. ML also acknowledges the Leidsch Kerkhoven-Bosscha Fonds for travel support. HO and FLS gratefully acknowledge the Swedish Natural Science Research Council (NFR) for financial support. We would like to thank the NCSA Astronomy Digital Image Library (ADIL) for providing images for this article. We thank the referee, Dr. K. Menten, for helpful comments.

References

Audinos P., Kahane C., Lucas R., 1994, A&A 287, L5
Bachiller R., Fuente A., Bujarrabal V., et al., 1997, A&A 319, 235
Becklin E.E., Frogel J.A., Hyland A.R., Kristian J., Neugebauer G., 1969, ApJ 158, L133
Bell M.B., 1993, ApJ 417, 305
Bieging J.H., Nguyen-Q-Rieu, 1989, ApJ 343, L25
Bieging J.H., Tafalla M., 1993, AJ 105, 576
Bieging J.H., Chapman B., Welch W., 1984, ApJ 343, L25
Bujarrabal V., Fuente A., Omont A., 1994, A&A 285, 247
Carlstrom J.E., Welch W.J., Goldsmith P.F., Lis D.C., 1990, AJ 100, 213
Cherchneff I., Glassgold A.E., 1993, ApJ 419, L41
Cherchneff I., Glassgold A.E., Mamon G.A., 1993, ApJ 410, 188
Claussen M.J., Kleinmann S.G., Joyce R.R., Jura M., 1987, ApJS 65, 385
Cohen M., Hitchon K., 1996, AJ 111, 962
Dayal A., Bieging J.H., 1993, ApJ 407, L37
Dayal A., Bieging J.H., 1995, ApJ 439, 996
van Dishoeck E. F., 1988, In: Millar T.J., Williams D.A. (eds.) Rate Coefficients in Astrochemistry. Kluwer, Dordrecht, p. 49
Doty S.D., Leung C.M., 1998, ApJ 502, 898
Fukasaku S., Hirahara Y., Masuda A., et al., 1994, ApJ 437, 410
Gensheimer P.D., Likkel L., Snyder L., 1995, ApJ 439, 445
Glassgold A.E., Lucas R., Omont A., 1986, A&A 157, 35
Green S., Thaddeus P., 1974, ApJ 191, 653
Groenewegen M.A.T., Whitelock P.A., 1996, MNRAS 281, 1347
Groenewegen M.A.T., Whitelock P.A., Smith C.H., Kerschbaum F., 1998, MNRAS 293, 18
Guélin M., Lucas R., Cernicharo J., 1993, A&A 280, L19
Guélin M., Lucas R., Neri R., 1997, In: IAU Symp. No. 170, p. 359
Guilloteau S., Omont A., Lucas R., 1987, A&A 173, 324
Guilloteau S., Delannoy J., Downes D., 1992, A&A 262, 624
Henkel C., Matthews H.E., Morris M., Terebey S., Fich M., 1985, A&A 147, 143
Huggins P.J., Glassgold A.E., 1982, ApJ 252, 201
Izumiura H., 1990, Ph.D. Thesis, Tokyo University
Izumiura H., Ukita N., Tsuji T., 1995, ApJ 440, 728
Izumiura H., Hashimoto O., Kawara K., Yamamura I., Waters L.B.F.M., 1996, A&A 315, L221
Jewell P.R., Snyder L.E., 1982, ApJ 255, L69
Jura M., Morris M., 1981, ApJ 251, 181
Kahane C., Gomez-Gonzalez J., Cernicharo J., Guélin, M., 1988, A&A 190, 167
Kerschbaum F., 1999, A&A 351, 627
Koike C., Hasegawa H., Manabe, A., 1980, Ap&SS 67, 495
Lambert D.L., Gustafsson B., Eriksson K., Hinkle K.H., 1986, ApJS 62, 373
Lucas R., Guélin M., 1999, In: Le Bertre T., Lèbre A., Waelkens C. (eds.) Proc. IAU Symp. 191, Asymptotic Giant Branch Stars. ASP, p. 305
Lucas R., Bujarrabal V., Guilloteau S., et al., 1992, A&A 262, 491
Lucas R., Guélin M., Kahane C., Audinos P., Cernicharo J., 1995, Ap&SS 224, 293
Marshall C.R., Leahy D.A., Kwok S., 1992, PASP 104, 397
MacKay D.S.S., Charnley S.B., 1999, MNRAS 302, 793
Millar T.J., Herbst E., 1994, A&A 288, 561
Neri R., Kahane, C., Lucas R., Bujarrabal V., Loup C., 1998, A&AS 130, 1
Ochsenbein F., 1997, Baltic Astronomy 6, 221
Olofsson H., 1996, In: van Dishoeck E.F. (ed.) Proc. IAU Symp. 178, Molecules in Astrophysics: Probes and Processes. Kluwer, Dordrecht, p. 45
Olofsson H., Eriksson K., Gustafsson B., Carlström U., 1993a, ApJS 87, 267
Olofsson H., Eriksson K., Gustafsson B., Carlström U., 1993b, ApJS 87, 305
Olofsson H., Lindqvist M., Nyman L.-Å., Winnberg A., 1998, A&A 329, 1059
Sahai R., Bieging J.H., 1993, AJ 105, 595

Schöier F.L., 2000, Ph.D. Thesis, Stockholm Observatory
Schöier F.L., Olofsson H., 2000a, A&A 359, 586
Schöier F.L., Olofsson H., 2000b, A&A submitted
Sopka R.J., Olofsson H., Johansson L.E.B., Nguyen-Q-Rieu, Zuckerman B., 1989, A&A 210, 78
Truong-Bach, Nguyen-Q-Rieu, Omont A., Olofsson H., Johansson L.E.B., 1987, A&A 176, 285
Truong-Bach, Nguyen-Q-Rieu, 1989, A&A 214, 267
Willacy K., Cherchneff I., 1998, A&A 330, 676
Wootten A., Nguyen-Q-Rieu, Truong-Bach, 1994, A&A 290, 198